Marquette University
e-Publications@Marquette

Master's Theses (2009 -) | Dissertations, Theses, and Professional Projects

Coupling into Waveguide Evanescent Modes with Applications in Electron Paramagnetic Resonance

Jason Walter Sidabras
Marquette University

Recommended Citation
Sidabras, Jason Walter, "Coupling into Waveguide Evanescent Modes with Applications in Electron Paramagnetic Resonance" (2010). *Master's Theses (2009 -)*. Paper 29.
http://epublications.marquette.edu/theses_open/29

COUPLING INTO WAVEGUIDE EVANESCENT MODES WITH APPLICATIONS IN ELECTRON PARAMAGNETIC RESONANCE

by
Jason W. Sidabras

A Thesis submitted to the Faculty of the Graduate School,
Marquette University,
in Partial Fulfillment of the Requirements for
the Degree of Master of Science.

Milwaukee, Wisconsin

May 2010

ABSTRACT
COUPLING INTO WAVEGUIDE EVANESCENT MODES WITH APPLICATIONS
IN ELECTRON PARAMAGNETIC RESONANCE

Jason W. Sidabras, B.S.

Marquette University, 2010

The use of analytical and numerical techniques in solving the coupling of evanescent modes in a microwave waveguide through slots can be optimized to create a uniform magnetic field excitation on axis within a waveguide. This work has direct applications in Electron Paramagnetic Resonance (EPR) where a 100 kHz time-varying magnetic field is incident on a sample contained in a microwave cavity. Typical cavity designs do not take into consideration the uniformity of the 100 kHz field modulation and assume it to be uniform enough over the sample region from quasi-static principles. This work shows otherwise and uses Ansoft (Pittsburgh, PA) High Frequency Structure Simulator (HFSS; version 12.0) and analytical dyadic Green's functions to understand the coupling mechanisms.

The techniques described in this work have shown that electromagnetic modes form in a rectangular and cylindrical waveguide domain even at frequencies a number of orders of magnitude below the waveguide cut-off frequencies. With slot thicknesses very small compared to a wavelength, Born's first approximation must be modified to account for a near field secondary wave. Additionally, mutual coupling between multiple slots has been shown to influence the overall magnetic field profile down the axis of the waveguide and in certain circumstances becomes more complex from interactions outside of the domain of the dyadic Green's functions.

A cylindrical TE_{01U} cavity resonant at W-band (94 GHz) is proposed where both the microwave magnetic field and, from this work, the 100 kHz time-varying magnetic field incident on the sample are uniform. This type of resonator is highly desirable in EPR experiments where inhomogeneity of magnetic fields affect signal purity. With the technology outlined in this work, experiments where a uniform field modulation amplitude is swept over the entire spectra to obtain pure absorption is feasible. This work advances the cutting edge of resonator design and enables new experiments to be performed at high field EPR.

ACKNOWLEDGEMENTS

This work as supported by grants EB001417 and EB001980 from the National Institute of Biomedical Imaging and Bioengineering of the National Institutes of Health.

I would like to thank Dr. James S. Hyde for the opportunity as an engineer at the Medical College of Wisconsin and the support for furthering my education at Marquette University. I would also like to thank Dr. James E. Richie for the numerous hours of discussion, guidance, and support throughout this work and Dr. Richard R. Mett for continuing to push me towards bettering myself.

Finally, I would like to thank my family and especially my girlfriend Emily for the support and needed push to finish this work.

I couldn't have done it without all of you.

TABLE OF CONTENTS

LIST OF FIGURES

LIST OF TABLES

Chapter 1: Introduction

In an Electron Paramagnetic Resonance (EPR) experiment, there are three fields incident on a differential sample volume to excite and measure magnetic resonance: i) a uniform static magnetic field from a super-conducting magnet, ii) the RF field in a microwave cavity, and iii) modulated field from an external coil added to the static magnetic field [1, 2, 3]. An illustration of these fields is found in Fig. 1.1. Here, the static and RF field, H_0 and H_1 respectively, are spatially perpendicular while a time-varying field is added parallel to the static magnetic field.

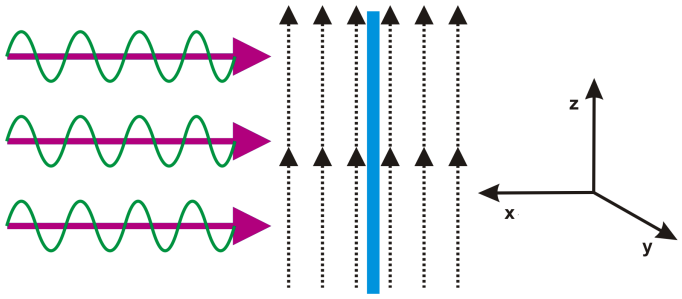

Figure 1.1: *There are three fields that are applied to a sample (solid blue) in an EPR experiment: i) the static magnetic field (purple), ii) the RF microwave field applied spatially perpendicular to the static magnetic field (dashed), and iii) the applied field modulation applied spatially parallel to the static magnetic field (green).*

Over the last five years research has been conducted to improve the uniformity of the RF magnetic field in a microwave cavity, where typically a cavity has a cosine dependence [4, 5, 6]. Using a waveguide section at cut-off over the region of interest and proper end-sections to tune the cavity to the cut-off frequency, a purely uniform field can be realized. The cavity is then immersed in a static magnetic field whose amplitude is swept slowly over the resonance condition.

These recent advancements of resonator technology using a waveguide section at cut-off achieve very good RF uniformity, yet there has been no literature to the author's knowledge about creating uniform field modulation by the techniques discussed in this work. Past and current literature assumes that the 100 kHz field modulation has such a large wavelength compared to the resonator body that it can be regarded as quasi-static [1, 7]. A *quasi-static* field is defined as a field which has no wave-like properties, such that

$\partial\overline{B}/\partial t = 0$. The penetration of field modulation into a resonator is described as "good enough" and is mostly assumed to be uniform in the waveguide cross-section and cosine down the axis of the sample. This work shows otherwise.

The use of commercially available finite-element modeling software, Ansoft (Pittsburgh, PA) High Frequency Structure Simulator (HFSS; version 12.0), provides an introduction to the understanding of the coupling of 100 kHz field modulation into a rectangular and cylindrical waveguide with slots cut perpendicular to the axis. For further understanding and insight of the coupling mechanisms and the evanescent modes associated with the coupling, analytical dyadic Green's functions are employed.

Two methods of field modulation are used in EPR. The first method is to slowly sweep the static magnetic field over the sample resonance line-width while a low frequency time-varying magnetic field is applied parallel to the static magnetic field [8]. The magnetic field modulation amplitude is definitely smaller than the half line-width of the sample resonance. This field modulation, typically 100 kHz, is used to shift the EPR signal off baseband and into harmonics of the field modulation frequency making it easier to detect. Field modulation improves receiver noise figures and avoids source phase noise. The frequency of 100 kHz is chosen as a frequency where cavity assemblies have few acoustic resonances from Lorentz forces on the resonator body. These acoustic resonances can cause vibrations that are carried through to the EPR signal. Historically, higher frequencies have been chosen but exhibit complex EPR effects that are not typically desired [9]. This work focuses on 100 kHz modulation frequency but can be applied to any frequency.

The second method is to choose the field modulation amplitude such that the entire line-width is swept through at the modulation frequency. The waveform can either be sinusoidal, saw tooth or triangular depending on the experiment being conducted. Sweeping the field modulation over the sample creates an undisturbed pure absorption signal. By collecting the real and imaginary data a pseudo-modulation technique can be used to generate the harmonic information [10]. Both methods need uniform field modulation along the sample line in order to properly identify the coefficients of the harmonics. From the harmonic information a signal can be obtained by Fourier

deconvolution [11, 12].

The field scan techniques and instrumentation for the second method of experiments are currently being developed and are on the cutting edge of EPR technology. With a uniform field modulation the absorption signal observed would come from the same position on the line-width and remove distortions caused by the derivative-like spectrum of field modulation. The technology described in this work will directly affect the feasibility of these techniques over other competing techniques such as frequency modulation in high field EPR. Although this work can be used at any practical frequency, W-band (94 GHz) is convenient as a frequency of importance to the author, due to the availability of state-of-the-art W-band instrumentation [13].

Between the understanding and intuition in this work and new strategies in resonator fabrication, a microwave cavity can be designed with both uniform RF field and uniform 100 kHz field modulation. This has a number of advantages in EPR. The first being that the sample has a uniform excitation along the axis of the sample, resulting in better quantitative data. The second advantage is the removal of "uncertainty" in the field modulation profile. Finally, this lends itself to experiments where the field modulation is part of the EPR physics.

Using numerical techniques a TE_{01U} cavity with uniform RF field is designed. Thirteen modulation slots are cut in the walls of the cavity parallel to the RF current to allow field modulation to penetrate the cavity. These slots are cut in such a way that the various slot depths excite magnetic fields within the cavity that produce an uniform 100 kHz field modulation excitation down the axis. To the author's knowledge, this is the first time multiple slots of different depths are used in a field modulation design as described. Optimizing the parameters needed to create such a design by hand has proven costly in resources. The main focus of this work is to understand the mechanism of coupling for field modulation slots and to use developed insight and tools to understand single and multiple slots interactions for both a rectangular and cylindrical cavity cross-section in order to determine design criteria for uniform field modulation down the axis of a cavity using cut slots.

This work is arranged in the following chapters: Chapter 2 establishes basic EPR

theory and the necessity of uniform field modulation. Then the theory needed to derive the dyadic Green's function associated with a slotted rectangular or cylindrical waveguide is formulated. From the dyadic Green's function equations, single-slot solutions are solved using Wolfram (Champaign-Urbana, IL) Mathematica (version 7.0.2) and compared to Ansoft (Pittsburgh, PA) High Frequency Structure Simulator (HFSS; version 12.0). The results of this work are presented in Chapter 3.

In Chapter 4, the single-slot solutions and translations to multiple slots is discussed. Chapter 4 also discusses successes and challenges to the dyadic Green's function method. A completed model and product is presented which incorporates both uniform field modulation and uniform RF field. Finally, Chapter 5 concludes the results and discusses future work directly relating to, or stemming from, the work presented here.

Chapter 2: Theory

2.1 Electron Paramagnetic Resonance

Electron Paramagnetic Resonance is a spectroscopic technique to measure free electrons in a sample, typically biological [1, 2, 3]. Samples containing a free electron have a complex susceptibility and do not retain magnetization without an applied static magnetic field. These materials are known as *paramagnetic* materials. Random alignment of the magnetization occurs when no external static magnetic field is present. With the presence of a magnetic field, the sample states go into either a high energy or low energy level according to Boltzmann statistics.

In 1946, Bloch introduced a series of differential equations to describe the phenomenon of magnetic resonance [14]. In the stationary solution to Bloch partial differential equations the RF magnetic susceptibility, $\chi' - i\chi''$, of a sample is described in dynamic terms through magnetic resonance. Here,

$$\chi' = \frac{1}{2}\chi_0 H_0 \frac{H - H_0}{H_1^2 \frac{T_1}{T_2} + (H - H_0)^2}, \text{ and} \tag{2.1}$$

$$\chi'' = \frac{\frac{1}{2}\chi_0 H_0}{\gamma} \frac{1}{H_1^2 T_1 + (H_0 - H)^2 T_2}, \tag{2.2}$$

where χ_0 is the static magnetic susceptibility, which is a bulk property of the sample and temperature of the system with a static magnetic field applied, γ is the gyromagnetic ratio ($2\pi 2.8$ rad/Gs for an electron), H_0 is the resonance static magnetic field strength, H is the swept static magnetic field strength, H_1 is the RF magnetic field strength, T_1 is the spin relaxation time and T_2 is the spin-spin relaxation time. The values T_1 and T_2 are characteristics of the sample. This solution to the Bloch equations assumes the microwave frequency is fixed and the static magnetic field strength, H, is swept around the neighborhood of magnetic resonance.

For a given microwave frequency there exists a magnetic resonance around the "neighborhood" of

$$\omega = \gamma |\overline{H}_0|, \tag{2.3}$$

where ω is the RF frequency in radians per second, γ is the gyromagnetic ratio ($2\pi 2.8$ rad/Gs for an electron), and H_0 is the static magnetic field intensity. Since it can be shown that sweeping frequency and holding the static magnetic field constant is equivalent to sweeping the static magnetic field and holding the frequency constant [1], the "neighborhood" around magnetic resonance can be defined as $|\omega - \omega_0| \ll \omega_0$ or $|H - H_0| \ll H_0$.

In the context of this work a typical experiment will have a sinusoidal continuous RF excitation on the sample as the static magnetic field is slowly swept in amplitude. When the RF fields are applied and the static magnetic field is swept through resonance, the lower energy state absorbs an electron and moves to the higher energy state changing the properties of the sample. The average absorbed power over the entire sample is quantified by [2]

$$P = \frac{\omega}{2}\chi'' \int \overline{H}_1 \cdot \overline{H}_1 dV_s. \tag{2.4}$$

Here ω is the microwave frequency in radians per second and $\overline{H}_1 \cdot \overline{H}_1$ is the magnitude squared of the applied RF magnetic field intensity in the sample volume, V_s. Most EPR experiments focus on detecting the microwave absorption, χ'', of the sample, but by adjusting the reference arm phase to 90 degrees out of phase with the signal arm, the paramagnetic dispersion attributed to χ' can be detected.

In an EPR experiment, the sample is placed in a microwave resonator and immersed in a static magnetic field, $\overline{H}_0$. The RF magnetic field of the standing waves in the microwave resonator, $\overline{H}_1$, is designed to be spatially perpendicular to the static magnetic field. One such microwave resonator is the cylindrical TE_{011} cavity.

The cylindrical TE_{011} cavity, pictured with field overlays in Fig. 2.1b, is constructed of a cylindrical waveguide terminated with two flat end-sections. The sample is placed down the center and the cavity is coupled by a long-slot iris [15].

The field configuration of the TE_{011} cavity is advantageous due to the maximum magnetic field concentrated in the center of the cavity, illustrated top of Fig. 2.1b. Additionally, the electric and magnetic field standing waves are separated in space in a microwave cavity which allows the sample to be placed in a maximum magnetic field and

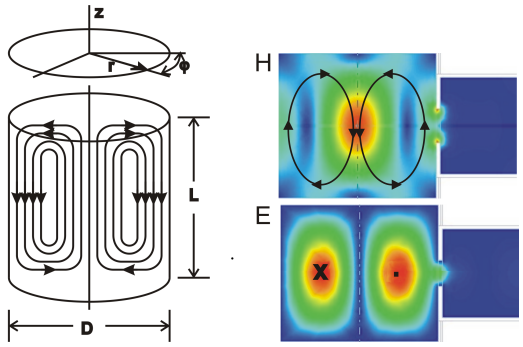

Figure 2.1: *Cylindrical TE_{011} Cavity. (a) In cylindrical coordinates, the electric field is oscillating in the ϕ-direction. A sample would be placed where ρ equals zero along the z-axis. As shown in (b), the magnetic field is a maximum there, while the electric field is a minimum.*

minimum electric field. This configuration has advantages in EPR experiments with lossy samples, such as aqueous phase proteins [13], by minimizing electric field incident on the sample.

The cavity is critically coupled to minimize the voltage standing-wave ratio (VSWR) within the waveguide onto some detection system [16]. As the static magnetic field is swept through the resonance condition, magnetic resonance slightly affects the losses and resonant frequency associated with the cavity by the change in the RF magnetic susceptibility, Eqns. 2.1 and 2.2, associated with the sample. When the cavity properties change, a mismatch is presented at the cavity iris causing an increase in VSWR on the transmission-line.

As the sample goes through resonance, the VSWR is measured and an absorption spectra is obtained. In general, an EPR signal can take on many forms depending on the sample properties. For simplicity, an EPR signal will be described using a Lorentzian line shape. If the frequency is maintained constant and the magnetic field strength is swept, the EPR line shape is described by

$$\phi(H) = \frac{y_m}{1 + 4\left(\frac{H - H_0}{\alpha_L}\right)^2}, \tag{2.5}$$

where α_L is the Lorentzian half-width in magnetic field units and H is the static magnetic

field strength and H_0 is the field strength solution to the resonant condition, and y_m is the peak amplitude of the line shape.

The instrumentation of a continuous-wave (CW) experiment *bridge* is outlined in Fig. 2.2. A basic EPR bridge consists of a microwave oscillator, typically set at a fixed frequency, split using a directional coupler into two main arms: a signal arm and a reference arm. The reference arm consists of an attenuator, phase shifter and delay line, which forms a controlled phase signal for down conversion and detection of the EPR signal. The signal arm uses a microwave circulator or directional coupler to direct the power to a critically tuned sample resonator and the reflection is directed through a circulator to a low-noise amplifier and mixer. When off resonance, no signal is present if the resonator is critically coupled and the system is properly tuned.

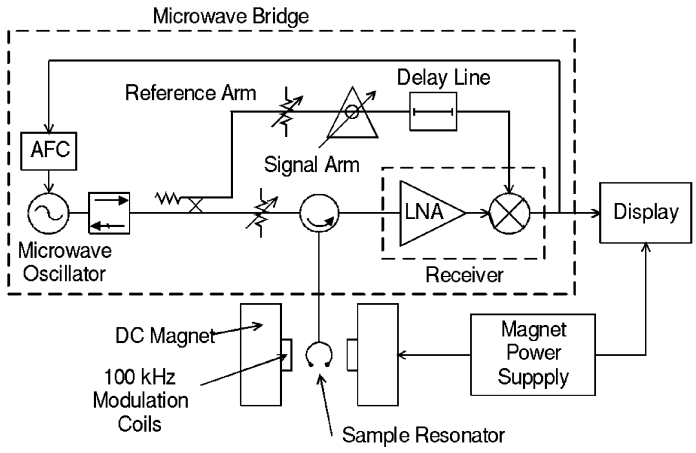

Figure 2.2: *A basic baseband EPR bridge consists of a microwave source, reference arm, microwave cavity and a receiver. For resonance to occur, a DC static magnet is slowly swept across resonance while a 100 kHz modulation field is applied to move the signal off of baseband.*

A low-noise amplifier (LNA) is placed as close as possible to the signal's return path, then the reference arm and signal arm signals are used to down convert to DC where an absorption signal is detected. This signal is placed on the display or digitally converted to be studied by a spectroscopist. An automatic frequency control (AFC) system is used to adjust the microwave oscillator frequency to that of the sample resonator if a relative frequency drift occurs.

The field modulation is spatially parallel to the static magnetic field such that the total magnetic field incident on the sample, $\overline{H}_t$, is

$$\overline{H}_t = H_0\hat{\mathbf{x}} + H_m \cos(\omega_m t)\hat{\mathbf{x}}, \tag{2.6}$$

where ω_m is the field modulation frequency in radians per second and H_m is the field modulation amplitude.

A number of ways exist to create field modulation signal parallel to the static magnetic field. First any wire in a loop near the resonant sample could be driven by a time-varying current source to produce magnetic fields. This method is popular in ENDOR where current "posts" are placed inside the microwave cavity [17]. This has its advantages in getting the field modulation at the sample, however vibrations are inherent in the design because the modulation coils are connected directly to the resonator.

Another method is the use of saddle coils. A saddle coil is a resonant coil that is placed outside the resonator body. It is typically driven by a voltage source and produces good field homogeneity. Since the coils are typically not attached to the resonator, direct vibrations are not transferred but there can be some vibrations caused by Lorentz forces on the cavity walls.

A method introduced by Varian is to use two coils for full spectra excitation. The first larger coil is driven strongly to sweep through the entire spectra while a second smaller coil is used to improve the homogeneity. This system was coupled with an additional field modulation coil at a much higher frequency in order to collect a derivative-like spectrum excitation.

This work will focus on using a Helmholtz pair of coils to excite a uniform field excitation over the cavity. A Helmholtz pair is two coils that are spaced a radius apart from each other. This produces homogeneity along the axis of the coils and, depending on the radius of the coils, uniformity in a finite plane.

There are a number of advantages to using a field modulation technique in detecting an EPR signal. First, a DC absorption signal, or baseband signal, is difficult to acquire due to a large noise figure caused by "$1/f$ noise" inherent in the mixer design and

associated with the mechanical junctions made to connect the diodes within the mixer to the input and reference ports [18]. Another challenge at baseband is that the crystal or digital detector system used to detect the signal is not optimal at DC.

By studying Bloch's equations it can be shown that applying field modulation to the static field is equivalent in most circumstances to frequency modulation. Therefore, field modulation produces sidebands at $\omega + n\omega_m$ allowing for proper filtering and detection. A signal detected from the first sideband of the field modulation scheme is a derivative-like process which makes it less susceptible to microwave source noises [2]. This derivative-like process is described in more detail in Fig. 2.3.

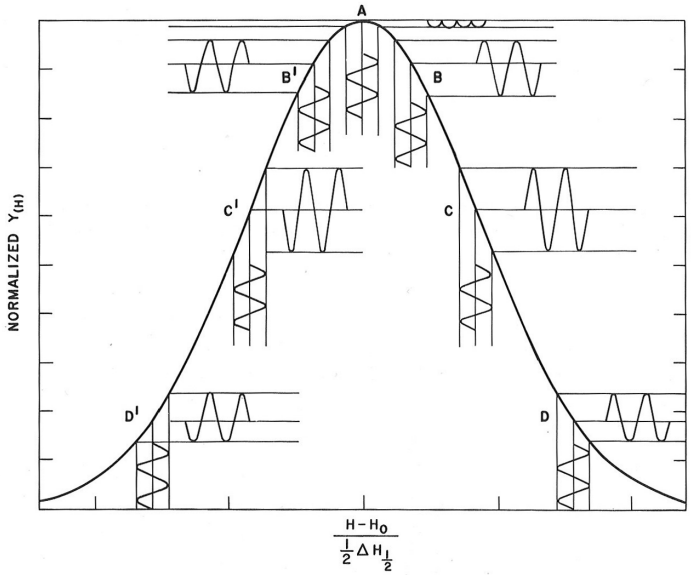

Figure 2.3: *A Lorentzian EPR absorption spectra is acted upon by field modulation. When the field modulation amplitude is definitely smaller than the spectra width a derivative-like spectrum is obtained. Reprinted from Ref. [1].*

Illustrated is the effect of field modulation on an EPR absorption of a Lorentzian line. The vertical axis is normalized signal strength and the horizontal axis is normalized magnetic field centered around the neighborhood of magnetic resonance. Field modulation is applied as the sinusoid varying the magnetic field strength. The result is the variation of the signal strength.

Figure 2.3 illustrates seven positions of the static magnetic field as it is swept through the line-width. Shown in D′, C′, and B′ labeled positions is the applied field

modulation sinusoid and the resulting amplitude variation at the field modulation frequency. At position A, the peak of the spectrum, the resultant amplitude variation is a null. The positions labeled B, C, and D are of opposite polarity of their prime counterparts and would represent the derivative in the negative portion of the spectra.

With small values of field modulation amplitude, compared to the line-width of the signal, the modulation creates pure derivative spectrum, illustrated in Fig. 2.4a. This spectrum contains no line broadening or second order effects caused by the modulation. However, the amplitude of the resultant signal is small.

By increasing the field modulation amplitude a derivative-like spectrum can be obtained with adequate signal strength, illustrated in Fig. 2.4b. However, in more complex EPR signals modulation can cause a loss of fine spectral structures of narrow components. Finally, when the field modulation amplitude approaches the order of the line-width the spectrum exhibits a significant broadening, illustrated in Fig. 2.4c.

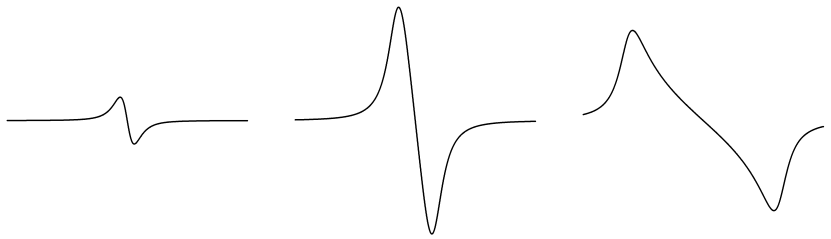

(a) **(b)** **(c)**

Figure 2.4: *Calculated detected signal using a field modulation scheme with a (a) small amplitude gives a pure Lorentzian derivative line shape; (b) typical amplitude gives a derivative-like line shape; and (c) modulation amplitude larger than the Lorentzian line-width gives a detected stretched line shape.*

To calibrate the field modulation amplitude, a spectroscopist uses a standard sample with a known line-width that is very narrow. Field modulation amplitude and phase is then calibrated for each resonator minimizing spectrum broadening. If the field modulation is not uniform over the sample volume, the "optimum" modulation amplitude and phase could be a combination of desired modulation effects and undesired effects, such as over modulation broadening. Since each macroscopic differential sample volume

would be excited by a different field modulation amplitude and phase, it would prove difficult to fully calibrate the modulation characteristics.

In other experiments, such as Saturation Transfer Spectroscopy, the field modulation is part of the physics of the experiment [19]. In such an experiment, the out of phase component of the field modulation signal is detected. To ensure proper phasing, a strong standard sample not exhibiting passage effects is used where the signal is nulled out in the out of phase channel. If the phase varies along the sample, there would be no phase in which the standard sample signal is fully canceled. In this case, the experiment could not be completed.

In the previous experiments, frequency modulation amplitude is a fraction of the total line-width and measures an approximation to the derivative of the line shape. Recent work in our laboratory at L-band (1 GHz) uses a triangular sweep at a 5 kHz rate with a large enough amplitude to sweep through the entire spectrum obtaining a pure absorption spectra instead of a derivative-like spectra. Uniform field modulation proves essential to the practicality of these techniques.

2.1.1 Field Modulation Coupling Techniques

There are three practiced techniques to allow field modulation through the walls of a cylindrical TE_{011} cavity: i) wire-wound structures, ii) wall plating thicknesses thin enough for 100 kHz penetration but thick enough for RF shielding, and iii) cutting slots parallel to wall currents in order to not disrupt RF currents but create potentials for 100 kHz penetration. These three techniques are outlined in Fig. 2.5. All three techniques assume a uniform 100 kHz Helmholtz coil excitation, yet the fields inside the metallic structure are found not to be uniform. This is due to perturbations of the field modulation magnetic field which arise from eddy-currents generated on the outside surface of the cavity.

The first technique for magnetic field penetration is a wire wound structure, illustrated in Fig. 2.5a. Hyde [7, 20] designed this structure at X-band (9.5 GHz) and later implemented it at Q-band (34 GHz). The structure consists of coated magnet wire wrapped around a Teflon rod and fastened together using polystyrene coating, while two end sections held the cavity together. Coupling of the RF fields is from an iris on the top

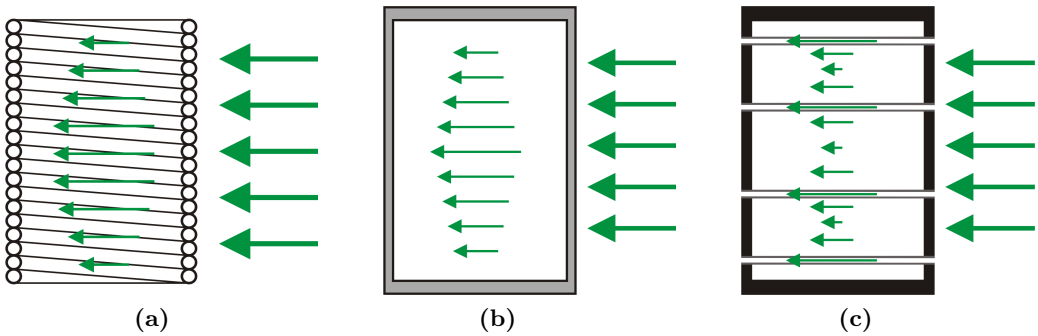

Figure 2.5: *Illustration of the three field modulation techniques are used in EPR. A wire wound structure (a) is created by wrapping thin gauge wire along a dielectric tube. The wires are then affixed by epoxy and the tube is removed. (b) A structure is made out of a dielectric, typically ceramic, and is plated with ten RF skin-depths of silver. (c) A solid silver structure with slots cut parallel to RF currents but perpendicular to field modulation eddy-currents.*

end section.

Using a wire wound cavity, the surface currents created by the incident time-varying magnetic field are sufficiently broken up allowing the field modulation to penetrate into the cavity. However, at X-band a 0.010 inch wire with 0.010 inch spacing was used and at Q-band 0.005 inch wire and spacing was used. This technique becomes impractical in high field EPR, where wire thicknesses and spacing would be less than 0.001 inches.

The second technique is to use the differences in skin depth to allow penetration of 100 kHz field modulation, illustrated in Fig. 2.5b. By using an electrically transparent material, such as graphite or ceramics, and silver plating the material with approximately ten RF skin-depths sufficiently low frequency field modulation can penetrate through, while creating an adequate conductive surface at RF frequencies. At X-band and higher, this technique works well in allowing field modulation penetration. An issue arises in high field EPR in plating the coupling iris. A long-slot iris at W-band for a TE_{011} cavity is around 0.05 mm. Plating in these small gaps is not practical.

The third technique is to construct a cavity out of solid silver and cut field modulation slots perpendicular to the resonator axis. A solid silver cavity has a number of advantages. Temperature stability and low acoustic resonances allow for a reduction in

baseline noises. Another advantage is a higher quality factor when the slots are cut parallel to RF currents in the cavity [21]. At higher frequencies the solid silver allows for coupling iris without having to worry about plating and the slots let adequate field modulation amplitude penetrate into the cavity [13, 22].

This technique has become more prominent in resonator design in our laboratory since the adoption of Electric Discharge Machining (EDM) manufacturing techniques. EDM is a fabrication process where a wire or plunger is put at a high voltage potential from the fabricated part and the material is arced away under an oil bath. EDM has shown to be an ultra precision fabrication process with cuts down to 0.05 mm and positional tolerances of 0.001 mm.

For testing field uniformity at lower RF frequencies, the modulation field can be probed using small (1 mm diameter) coils. Although useful in calibration and field testing, these coils do not probe the whole sample cross-section. Additionally, the probe itself would modify the fields. In the case of higher frequencies and "true" field profiles, numerical and analytical analysis lends itself as the best solution for characterizing the field profile.

2.1.2 Proposed Uniform Field Modulation Cavity Design

A proposed microwave cavity can be found in Fig. 2.6a. Here, the cavity is a cylindrical TE_{011} where the central region of interest has been designed to be at cut-off resulting in a uniform microwave magnetic field [4, 5, 6]. This kind of cavity is denoted as a cylindrical TE_{01U} cavity.

In order to allow field modulation into the cavity, thirteen slots are cut into the side of the wall. This proposed cavity uses a novel scheme of varying the depth of the slots to shape the incident field modulation along the axis. Using Ansoft HFSS the slot depths were optimized to create a uniform incident field modulation, shown in Fig. 2.6b. Each simulation took approximately 20 minutes and about 30 simulations were completed where the slot depths were varied by hand to obtain a uniformity of 3.6% deviation from unity. To the author's knowledge, this is the first time such a field modulation design has been described.

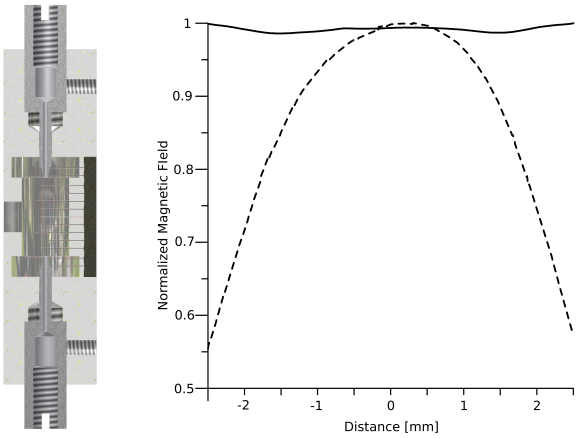

(a) **(b)**

Figure 2.6: *(a) A cylindrical TE_{01U} cavity optimized for both uniform microwave magnetic field. The magnetic field profile has been optimized using Ansoft HFSS. Thirteen slots are cut into the cavity to create a more uniform profile over the region of interest. (b) Shows the comparison between the optimized profile (solid) and a typical profile with slots of the same depth (dashed).*

To create a uniform magnetic field on the axis of the cavity, a large number of parameters need to be defined. In the construction of the proposed cavity such parameters as the number of slots, the location of the slots, and the depth of the slots are defined by intuition, leading to good success after many iterations. To refine the design process, an analytical formulation is developed here that models the fields due to slots. It is expected that the results of this investigation will provide insight into these parameters.

Ansoft allows the full solution to be computed with little understanding to the coupling mechanisms of the field modulation penetration and the interactions between each slot. To build a better intuition and understanding of the interactions between the magnetic field incident on the cavity and the slots, and between the slots themselves, an analytic solution is developed.

2.2 Electromagnetic Solutions

Electromagnetic solutions can be constructed in a variety of ways. One common practice is to use vector potentials as tools to solve the electromagnetic fields from sources, illustrated by following *Path 1* in Fig. 2.7. Notation is $\overline{A}$ for the *magnetic vector potential*

and $\overline{F}$ for the *electric vector potential*. Additionally, an *electric scalar potential*, Φ, can be defined. Vector potentials, known as Hertz potentials, are also used and are derivable from $\overline{A}$ and Φ [23]. Another way to solve electromagnetic boundary-value problems is to use a mathematical kernel that contains all boundary information. This is depicted as *Path 2* in Fig. 2.7, where sources are transformed into solutions by a linear operator.

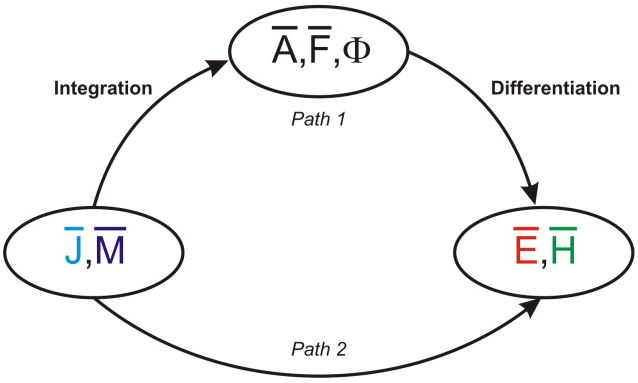

Figure 2.7: *Illustration of the methods for computing electromagnetic fields from electric and magnetic sources. Two common paths exist: Path 1 transforms sources to vector potentials using integration techniques. Then, since the vector potentials and sources have the same vector direction, a differentiation mathematically manipulates the vector potentials into the field solutions. Path 2 uses a closed-form function to solve the fields directly by the sources.*

2.2.1 Vector Potentials

Time-harmonic electric and magnetic fields, $e^{-i\omega t}$, are assumed throughout the formulation of the problem and solutions. First, consider Maxwell's equations in a homogeneous and charge free medium:

$$\nabla \times \overline{E} = -\overline{M} + i\omega\mu\overline{H} \text{ and} \tag{2.7}$$

$$\nabla \times \overline{H} = \overline{J} - i\omega\epsilon\overline{E}, \tag{2.8}$$

where $\overline{E}$ and $\overline{H}$ are the electric and magnetic field intensities, respectively. The electric and magnetic flux densities are defined where $\overline{D} = \epsilon\overline{E}$ is the electric flux density, while $\overline{B} = \mu\overline{H}$ is the magnetic flux density. The sources can be either magnetic current, $\overline{M}$, or electric current, $\overline{J}$. The definitions $\overline{B} = \nabla \times \overline{A}$ and $\overline{D} = \nabla \times \overline{F}$, are substituted into

Maxwell's equations, separately, resulting in a transformation to express the solution in the vector potential form.

This derivation is described in detail in many references [24, 25, 26, 27, 28]. Most notably, Harrington [24] and Tai [25] express the vector potential relationships as

$$\boldsymbol{\nabla}^2\overline{A} + k^2\overline{A} = -\mu\overline{J}, \text{ and} \tag{2.9}$$

$$\boldsymbol{\nabla}^2\overline{F} + k^2\overline{F} = -\epsilon\overline{M}, \tag{2.10}$$

where k is the wave number and $k^2 = \omega^2\mu\epsilon$. Equations 2.9 and 2.10 are known as inhomogeneous Helmholtz equations, and their solutions are known as *wave potentials*. Wave potentials are generally created by multiplying the source and propagator and integrating:

$$\overline{A}(\overline{r}) = \mu \iiint \overline{J}(\overline{r}')g_0(\overline{r};\overline{r}')dV', \text{ and} \tag{2.11}$$

$$\overline{F}(\overline{r}) = \epsilon \iiint \overline{M}(\overline{r}')g_0(\overline{r};\overline{r}')dV'. \tag{2.12}$$

where the scalar free-space propagator or kernel for *unbounded homogeneous mediums* is used:

$$g_0(\overline{r};\overline{r}') = \frac{e^{ik|\overline{r}-\overline{r}'|}}{4\pi\left|\overline{r}-\overline{r}'\right|}, \tag{2.13}$$

where $\overline{r}$ is the observation point and $\overline{r}'$ is the source point in a Cartesian coordinate system.

From the wave potentials, the second step following *Path 1* in Fig 2.7 is performed. Both $\overline{A}$ and $\overline{F}$ are vectors in the same direction as the sources, $\overline{J}$ and $\overline{M}$, respectively. The solutions, $\overline{E}$ and $\overline{H}$, are not necessarily in the same direction as the sources. The solutions $\overline{H}$ and $\overline{E}$ are derived from $\overline{J}$ through $\overline{A}$, and $\overline{M}$ through $\overline{F}$ resulting in the total field solution

$$\overline{H}(\overline{r}) = \frac{1}{\mu}\boldsymbol{\nabla}\times\overline{A}(\overline{r}) + i\omega\overline{F}(\overline{r}) + i\frac{1}{\omega\mu\epsilon}\boldsymbol{\nabla}\left[\boldsymbol{\nabla}\cdot\overline{F}(\overline{r})\right], \text{ and} \tag{2.14}$$

$$\overline{E}(\overline{r}) = i\omega\overline{A}(\overline{r}) + i\frac{1}{\omega\mu\epsilon}\boldsymbol{\nabla}\left[\boldsymbol{\nabla}\cdot\overline{A}(\overline{r})\right] + \frac{1}{\epsilon}\boldsymbol{\nabla}\times\overline{F}(\overline{r}). \tag{2.15}$$

Depending on the problem at hand, the resultant total fields are found using either $\overline{A}$, $\overline{F}$ or a combination of both vector potentials. The convenience of *Path 1* in Fig. 2.7 is that the vector potentials lie parallel to the sources by way of an unbounded homogeneous scalar free-space kernel; however, this method relies on assumptions that drastically simplify the problem.

The most notable assumption is the use of the scalar free-space kernel for *unbounded homogeneous media*. In other words, the kernel, or Green's function, is created in such a way that physical obstacles in the problem must be mathematically removed before the solution can be "propagated". Although this method has a number of uses in antenna and scattering theory, it is inadequate when inside a waveguide. For cases where the boundary conditions and sources are contained in a bounded inhomogeneous medium, *Path 2* in Fig. 2.7 is used.

2.2.2 Boundary Conditions

In boundary-value problems, there typically exists some partial-differential linear kernel acting upon a source which describes the system. The kernel, or Green's function, contains a set of functions that satisfy boundary conditions. These boundary conditions can be described as fixed values or vectors on the spacial bounds of a problem. Two types of boundary conditions typically exist in electromagnetic problems: Dirichlet and Neumann. *Dirichlet boundary conditions* are defined as

$$\hat{\mathbf{n}} \times \overline{\psi} = \overline{\alpha}, \tag{2.16}$$

where the function, $\overline{\psi}$, is acted upon a unit vector normal to the boundary, $\hat{\mathbf{n}}$, and has a value of $\overline{\alpha}$ at that boundary. The electric field along a perfect electric conducting (PEC) boundary, where the tangential field is strictly zero on the boundary due to an image field that is formed mirroring the applied electric field is an example of Eqn. 2.16.

Neumann boundary conditions are defined as

$$\hat{\mathbf{n}} \times \boldsymbol{\nabla} \times \overline{\psi} = \overline{\alpha} \tag{2.17}$$

where the derivative of the function, $\boldsymbol{\nabla} \times \overline{\psi}$, is transverse to the boundary, $\hat{\mathbf{n}}$, and has a value of $\overline{\alpha}$ at that boundary. The magnetic field along a PEC boundary, where the derivative of the field is strictly zero on the boundary, is an example of Eqn. 2.17.

A problem can be described as either open or closed. An *open* bounded problem has at least one dimension extending toward infinity, while a *closed* bounded problem is completely bounded by explicit boundary conditions.

In the construction of a boundary-value problem, the boundary conditions will be explicitly used to to determine the kernel needed for a solution using *Path 2* in Fig. 2.7. Two types of kernels exist: eigenfunction (or modal) and explicit kernels, which are examined next.

2.2.3 Eigenfunctions and Eigenvalues

Eigenfunctions and eigenvalues are mathematical characterizations of solutions to boundary-value problems using a series of orthogonal functions. An *eigenfunction*, ψ, is any non-zero function that when a linear operation, $\mathscr{L}$, is performed, the eigenfunction is returned multiplied by a scalar, k, known as an *eigenvalue*. This can be expressed mathematically as

$$\mathscr{L}\psi = k\psi. \tag{2.18}$$

The set of eigenfunctions used to define a solution can be shown to be a complete set of basis functions. A "complete" set is defined as a series of functions that can fully express a piecewise continuous function. Mathematically, this is defined as

$$\widetilde{F} \widetilde{=} \sum_{n=0}^{N_0} A_n \psi_n. \tag{2.19}$$

When there exists a finite number, N_0, such that for $N > N_0$ the mean square error between the original function and $\widetilde{F}$ is negligible; the series is said to converge. All orthogonal eigenfunctions that are solutions to the Helmholtz wave equation have been shown to be complete [26].

The solution of the eigenfunction problem is highly dependent on boundary

conditions and it is crucial to choose the right eigenfunctions to ensure convergence of the solution as n approaches infinity. Eigenvalues are infinite in number, extending from the lowest, k_0 to the maximum k_n which results in an acceptable convergence. In the case of the Helmholtz wave equation, Table 2.1 displays a list of some possible eigenfunctions that are acceptable solutions.

Table 2.1: *Possible solutions to the Helmholtz wave equation for a given set of boundary conditions*

Description	**Boundary Condition**	**Eigenfunction**
Rectangular standing wave, Dirichlet boundary conditions	$\hat{\mathbf{n}} \times \overline{E} = 0$	$sin(k_x x)$
Rectangular standing wave, Neumann boundary conditions	$\hat{\mathbf{n}} \times \boldsymbol{\nabla} \times \overline{E} = 0$	$cos(k_x x)$
Cylindrical standing wave, Neumann boundary conditions	$\hat{\mathbf{n}} \times \overline{E} = 0$	$J_n(k_x x)$
Cylindrical standing wave, Neumann boundary conditions	$\hat{\mathbf{n}} \times \boldsymbol{\nabla} \times \overline{E} = 0$	$J'_n(k_x x)$
Propagating waves	-	$e^{ik_x x}$
Diffusion	-	$e^{k_x x}$

The Ohm-Rayleigh method uses eigenfunctions exclusively in the formulation of Green's functions over a domain, Ω. The advantage of using orthogonal eigenfunctions is that

$$(k_n - k_m) \int \psi_n \cdot \psi_m d\Omega = 0, \quad \text{where } n \neq m \text{ and} \tag{2.20}$$

where k_n and k_m are distinct. By using the orthogonality of eigenfunctions, the coefficients of the series can be determined. If ψ_n are defined such that

$$\int \psi_n \psi_n d\Omega = 1, \tag{2.21}$$

then an orthonormal set is formed.

Separation of Variables and Three-Dimensional Construction

Eigenfunctions were described over a one-dimensional domain in the previous section. But by the method of separation of variables, general solutions for the Helmholtz wave equation can be constructed for three-dimensional orthogonal coordinate systems. In

general, use of e_1, e_2, and e_3 will denote such a coordinate system. In practice, the coordinate system is rectangular, cylindrical, or one of nine other three-dimensional orthogonal coordinate systems that have been shown to be valid using the separation of variables method [26].

The generalized Helmholtz wave equation is defined as

$$\boldsymbol{\nabla}^2\psi + k^2\psi = 0. \tag{2.22}$$

The method of separation of variables is to assume a solution for ψ that is the product of three separate functions, one for each coordinate, such that

$$\psi = A(e_1)B(e_2)C(e_3). \tag{2.23}$$

Inserting Eqn. 2.23 into Eqn. 2.22 and defining $k_1^2 + k_2^2 + k_3^2 = k^2$ form three separated harmonic equations, generalized in Cartesian coordinates as

$$\frac{\partial^2 A(e_1)}{\partial e_1^2} + k_1^2 A(e_1) = 0, \tag{2.24}$$

$$\frac{\partial^2 B(e_2)}{\partial e_2^2} + k_2^2 B(e_2) = 0, \text{ and} \tag{2.25}$$

$$\frac{\partial^2 C(e_3)}{\partial e_3^2} + k_3^2 C(e_3) = 0. \tag{2.26}$$

Solutions to these harmonic equations are called *harmonic functions*. A list of some possible solutions has already been given in Table 2.1. With harmonic functions, the eigenfunctions, ψ, can be generated such that

$$\psi = \sum_{k_1}\sum_{k_2} \alpha_{k_1 k_2} h_1(k_1 e_1) h_2(k_2 e_2) h_3(k_3 e_3), \tag{2.27}$$

where h is a properly chosen eigenfunction for the bounded problem and k_i is the corresponding eigenvalue. In this definition, $\alpha_{k_1 k_2}$ is the normalizing constant found using the Ohm-Rayleigh method. It is important to note that two eigenvalues are free parameters, and the third, propagation eigenvalue k_3, is determined by the propagation

constant k via the separation equation,

$$k_1^2 + k_2^2 + k_3^2 = k^2. \tag{2.28}$$

.

2.2.4 Green's Functions

Green's functions are mathematical tools used to solve inhomogeneous boundary-value problems directly from the sources, illustrated by *Path 2* in Fig. 2.7. In general, a solution to the partial differential equation is obtained by probing the system with an impulse. The response of the impulse contains all boundary and medium information for the particular problem. The general solution is expressed as an integral over the Green's function multiplied by the appropriate forcing function. The forcing function can be a source and/or a boundary function. Morse and Feshbach [28] describe a Green's function as:

> [...] a solution for a case which is homogeneous everywhere except at one point.

The "one point" is an impulse forcing function on a particular problem, and the integral is the convolution of a general forcing function with the impulse response. In general, a scalar Green's function, $g(\overline{r};\overline{r}')$, takes the form of

$$\mathscr{L}g(\overline{r};\overline{r}') = \delta(\overline{r} - \overline{r}'), \tag{2.29}$$

where $\mathscr{L}$ is a linear differential operator, $\overline{r}'$ is a "source" point in space, and $\overline{r}$ is an observation point in the solution space not including $\overline{r}'$. The Dirac delta function, δ, is defined by

$$\delta(\overline{r} - \overline{r}') = 0, \quad \overline{r} \neq \overline{r}', \text{ and} \tag{2.30}$$

$$\int_{-\infty}^{+\infty} \delta(\overline{r} - \overline{r}')d\Omega = 1. \tag{2.31}$$

where Ω is an arbitrary domain. The delta function allows specification of an exact point in space where an applied "source" is located. It is important to understand that the Dirac delta function is a "generalized" function with the properties expressed in Eqns. 2.30 and 2.31. A singularity exists when $\overline{r} = \overline{r}'$.

Green's second theorem is used directly as the underlying mathematics to find the Green's function solution of a problem. Green's second theorem can be derived from Gauss's theorem:

$$\int_{\Omega} \boldsymbol{\nabla} \cdot \overline{F} d\Omega = \oint_{\sigma} \overline{F} \cdot d\overline{\sigma}, \tag{2.32}$$

where

$$\overline{F} = \mathscr{G} \boldsymbol{\nabla} \psi - \psi \boldsymbol{\nabla} \mathscr{G}, \tag{2.33}$$

where σ is a closed surface and Ω is a solution domain. Inserting Eqn. 2.33 into Eqn. 2.32 yields the scalar Green's second theorem,

$$\int_{\Omega} (\psi \boldsymbol{\nabla}^2 \mathscr{G} - \mathscr{G} \boldsymbol{\nabla}^2 \psi) d\Omega = \oint (\psi \boldsymbol{\nabla} \mathscr{G} - \mathscr{G} \boldsymbol{\nabla} \psi) \cdot d\sigma. \tag{2.34}$$

Since $\boldsymbol{\nabla}^2 \mathscr{G}$ results in a term proportional to $\delta(\overline{r} - \overline{r}')$, the first term results in $\psi(\overline{r})$. The second term on the left side of Eqn. 2.34 represents the integral over the sources. The right side of the equation represents integration over the boundary conditions. Either ψ or $d\psi/d\overline{n}$ is specified on the boundary. Depending on the boundary conditions and boundary sources, either $\mathscr{G}$ or $\boldsymbol{\nabla}\mathscr{G}$ is zero. From Eqn. 2.34, a Green's function can be constructed for a given boundary-value problem.

Two types of Green's functions can be constructed: i) a finite series of explicit functions or ii) an infinite series of complete orthonormal functions. The first method uses a known mathematical response of the system to derive a solution. The second method is referred to as the Green's function using *eigenfunction expansion* or a *modal* Green's function.

In the previous example, Eqn. 2.13 was used to describe a wave radiating into free space. The kernel, $g_0(\overline{r}; \overline{r}')$, is known as the free-space Green's function and can be

derived by solving the Helmholtz wave equation:

$$\boldsymbol{\nabla}^2 g_0(\overline{r};\overline{r}') + k^2 g_0(\overline{r};\overline{r}') = -4\pi\delta(\overline{r}-\overline{r}'). \tag{2.35}$$

Since an outgoing wave is unbounded and infinite, it must satisfy the radiation condition:

$$\lim_{\overline{r}\to\infty} \left|\overline{r}-\overline{r}'\right| \left(\frac{\partial g_0(\overline{r};\overline{r}')}{\partial \left|\overline{r}-\overline{r}'\right|} - ikg_0(\overline{r};\overline{r}')\right) = 0. \tag{2.36}$$

Using the radiation condition in Eqn. 2.36 yields the free-space Green's function described in Eqn. 2.13. This method utilizes an explicit function, $e^{ik|\overline{r}-\overline{r}'|}/4\pi\left|\overline{r}-\overline{r}'\right|$, for an impulse response. The formulation assumes that the boundary condition is at infinity, which is useful only if there exists an infinite radiation boundary. In contrast, if boundary conditions limit the domain, it is often advantageous to use a set of orthonormal functions, or *eigenfunctions*, to describe the impulse response of the system.

For instance, assume a string of wire is along the $\hat{\mathbf{x}}$ direction connected at the origin and at point a. Again, the Helmholtz equation is used to describe the wave vibrations of the wire along the $\hat{\mathbf{x}}$ direction, denoted by

$$\frac{\partial^2\psi_n(x)}{\partial x^2} + k_n^2\psi_n(x) = 0, \text{ and} \tag{2.37}$$

$$\frac{\partial^2 g_0(x;x')}{\partial x^2} + k^2 g_0(x;x') = -4\pi\delta(x-x'). \tag{2.38}$$

Here $\psi_n(x)$ are the eigenfunctions with corresponding eigenvalues, k_n^2, and the Green's function, $g_0(x;x')$, takes the same form. Since the domain is $\Omega(0 \le x \le a)$, the solution—and, therefore, the eigenfunctions—must satisfy the boundary conditions $\psi_n(0) = \psi_n(a) = 0$. To satisfy the boundary conditions $\psi_n(0) = \psi_n(a) = 0$, the sinusoidal coefficient k_n must be properly chosen so that the sine function is zero, such that:

$$k_n = \tfrac{n\pi}{2}, \quad \text{where } n = 0, 1, 2, 3, \ldots. \tag{2.39}$$

Thus, the Green's function is constructed as

$$g_0(x) = \sum_n A_n \sin(k_n x), \tag{2.40}$$

where the constants A_n and k_n must satisfy the boundary conditions and the Helmholtz equation. Inserting Eqn. 2.40 into 2.38 results in

$$\sum_n \frac{\partial^2 A_n \sin(k_n x)}{\partial x^2} + k^2 A_n \sin(k_n x) = -4\pi\delta(x - x'). \tag{2.41}$$

The eigenfunctions form a complete orthonormal set, and, thus,

$$\int_\Omega \psi_n \psi_m d\Omega = \begin{cases} 1 & n = m \\ 0 & n \neq m \end{cases}. \tag{2.42}$$

Next, the *Ohm-Rayleigh method* is used to find the coefficient A_m by multiplying both sides of Eqn. 2.41 by ψ_m and integrating over the domain, Ω. This forms the constant coefficient

$$A_n = \frac{4\pi \sin(\alpha_n x')}{k^2 - \alpha_n^2}. \tag{2.43}$$

The complete modal Green's function for a string lying in the $\hat{\mathbf{x}}$ direction bounded at the origin and at length a is

$$g_0(x; x') = \sum_{n=1}^{\infty} \frac{4\pi \sin(\frac{n\pi}{2}x) \sin(\frac{n\pi}{2}x')}{(\frac{n\pi}{2})^2 - k^2}, \tag{2.44}$$

where the solution can be computed to the desired precision by increasing the number of eigenvalues, n.

Properties of Green's Functions

With the derivation of Eqn. 2.44, the properties of a Green's function can be explicitly described. The first property concerns the *reciprocity theorem.* The reciprocity theorem states that if one point is observed and another is excited, the solution is the same as if

the position of the observation and excitation point are exchanged:

$$g_0(x;x') = g_0(x';x). \tag{2.45}$$

This property can be demonstrated by the formulation of the coefficient A_n, as in Eqn. 2.43, using the Ohm-Rayleigh method. Since the coefficients depends on x'; A_n replicates this orthogonal eigenfunction, resulting in the required symmetry. Therefore, the source point and observation point can be interchanged with no effect on the solution.

The second property of a Green's function concerns the solution space. A Green's function must make it possible to obtain a solution to inhomogeneous or homogeneous solutions by the superposition of all source points. For instance, using the previous example, a string is excited in the $\hat{\mathbf{x}}$ direction by an impulse source at x_0,

$$\psi(x) = \int_\Omega \sum_n \frac{4\pi \sin(\frac{n\pi}{2}x)\sin(\frac{n\pi}{2}x')}{(\frac{n\pi}{2})^2 - k^2}\delta(x' - x_0)d\Omega, \tag{2.46}$$

or at set points, x_j, where $j = 0, 1, 2, 3$,

$$\psi(x) = \int_\Omega \sum_{j=0}^{3}\sum_{n=0}^{\infty} \frac{4\pi \sin(\frac{n\pi}{2}x)\sin(\frac{n\pi}{2}x')}{(\frac{n\pi}{2})^2 - k^2}\delta(x' - x_j)d\Omega. \tag{2.47}$$

The last property of a Green's function is that for inhomogeneous boundary conditions, there is a discontinuity at the boundary. This limits the solution space to inside the appropriate domain. In Gauss's second theorem, Eqn. 2.34, the limitation to the domain is shown in the left side of the equation.

2.2.5 Dyadic Green's Functions

Both the unbounded discrete, Eqn. 2.13, and the bounded modal, Eqn. 2.44, examples use a scalar Green's function as the "propagator" or kernel to the solution space. Although the solutions are expressed as vectors, they are easily obtained from a scalar kernel acting on a known source. For a vector solution the kernel must be a vector operator "propagating" all three components of the vector in the orthogonal coordinate system.

With the use of vectors as source and boundary conditions, vector operators called dyadics [25, 28, 29, 30] must be used. The *dyadic* is a tensor operator that linearly transforms one vector to another vector. The new vector is related to the original vector by the coefficients in the tensor. A dyadic form of Green's second theorem, Eqn. 2.34, includes the dyadic boundary conditions and sources to produce a dyadic Green's function operator. A dyadic tensor operator, denoted by a double vector notation, $\overline{\overline{\mathscr{G}}}$, can be described as

$$\overline{\overline{\mathscr{G}}} = \sum_i \sum_j \alpha_{ij} \hat{\mathbf{e}}_i \hat{\mathbf{e}}_j, \tag{2.48}$$

where $\hat{\mathbf{e}}_i$ and $\hat{\mathbf{e}}_j$ represent the orthogonal unit vectors in the coordinate system and α is a complex mathematical coefficient that can be a function of x, y, z or, in general, e_1, e_2, e_3. A dyadic can also be described as the *Kronecker product*, or outer product, of two vectors. For example, the Kronecker product of vectors $\overline{\beta}(x,y,z)$ and $\overline{\gamma}(x,y,z)$ results in

$$\overline{\beta}(x,y,z) \otimes \overline{\gamma}(x,y,z) = \begin{bmatrix} \beta_x\gamma_x\hat{\mathbf{x}}\hat{\mathbf{x}} & \beta_x\gamma_y\hat{\mathbf{x}}\hat{\mathbf{y}} & \beta_x\gamma_z\hat{\mathbf{x}}\hat{\mathbf{z}} \\ \beta_y\gamma_x\hat{\mathbf{y}}\hat{\mathbf{x}} & \beta_y\gamma_y\hat{\mathbf{y}}\hat{\mathbf{y}} & \beta_y\gamma_z\hat{\mathbf{y}}\hat{\mathbf{z}} \\ \beta_z\gamma_x\hat{\mathbf{z}}\hat{\mathbf{x}} & \beta_z\gamma_y\hat{\mathbf{z}}\hat{\mathbf{y}} & \beta_z\gamma_z\hat{\mathbf{z}}\hat{\mathbf{z}} \end{bmatrix}. \tag{2.49}$$

Since $\hat{\mathbf{e}}_i\hat{\mathbf{e}}_j \neq \hat{\mathbf{e}}_j\hat{\mathbf{e}}_i$, the functions are defined where the vector is acting on the dyad as the *anterior* product, $\overline{\alpha}\overline{\overline{\mathscr{G}}}$, and where the dyad is acting on the vector, as the *posterior* product, $\overline{\overline{\mathscr{G}}}\overline{\alpha}$. The anterior and posterior products are only equal in a symmetric dyad.

One special case of a symmetric dyad is the dyadic identity, $\overline{\overline{I}}$, where

$$\overline{\overline{I}} = \sum_i \delta_{ij} \hat{\mathbf{e}}_i \hat{\mathbf{e}}_i = \hat{\mathbf{x}}\hat{\mathbf{x}} + \hat{\mathbf{y}}\hat{\mathbf{y}} + \hat{\mathbf{z}}\hat{\mathbf{z}}. \tag{2.50}$$

Here δ_{ij} is known as the Kronecker delta function and is defined by

$$\delta_{ij} = \begin{cases} 1, & i = j \\ 0, & i \neq j \end{cases}. \tag{2.51}$$

Similar to matrix multiplication of the dyadic identity on another matrix, a scalar product (Eqn. A-6) between a vector and the dyadic identity results in that vector. A full

list of dyadic properties can be found in the appendix and will be referenced during formulation of the dyadic kernel.

The dyadic Green's function has the same properties as its scalar counterpart: i) it must satisfy the reciprocity theorem, ii) it will generate the complete solution from boundary conditions and sources, and iii) it results in solutions only valid within the boundary and has a discontinuity at the source point.

Dyadic Green's Functions of the Magnetic and Electric Type

As described earlier in *Path 2* of Fig. 2.7, the solution to an electromagnetic boundary-value problem is directly formulated by the method of dyadic Green's functions. For electric and magnetic current point sources, the following equalities are formed:

$$i\omega\mu_0\overline{\overline{J}} = \overline{\overline{I}}_J\delta(\overline{r}-\overline{r}') \text{ and} \tag{2.52}$$

$$i\omega\epsilon_0\overline{\overline{M}} = \overline{\overline{I}}_M\delta(\overline{r}-\overline{r}'), \tag{2.53}$$

where $\overline{\overline{J}}$ and $\overline{\overline{M}}$ are the dyadic form of the electric and magnetic current point sources. For point sources, the dyadic electric and magnetic Green's functions can be created. The relationships can be described as

$$\overline{\overline{E}} = \overline{\overline{G}}_e \text{ and} \tag{2.54}$$

$$i\omega\mu_0\overline{\overline{H}} = \overline{\overline{G}}_m, \tag{2.55}$$

where $\overline{\overline{E}}$ and $\overline{\overline{H}}$ are the dyadic form of the electric and magnetic fields, respectively. Each dyad is described by the general form of Eqn. 2.48. Maxwell's equations can then be written in a dyadic form such that

$$\boldsymbol{\nabla}\times\overline{\overline{G}}_e = -\overline{\overline{I}}_M\delta(\overline{r}-\overline{r}') + \overline{\overline{G}}_m, \tag{2.56}$$

$$\boldsymbol{\nabla}\times\overline{\overline{G}}_m = \overline{\overline{I}}_J\delta(\overline{r}-\overline{r}') + k^2\overline{\overline{G}}_e, \tag{2.57}$$

$$\boldsymbol{\nabla}\cdot\overline{\overline{G}}_e = 0, \text{ and} \tag{2.58}$$

$$\boldsymbol{\nabla}\cdot\overline{\overline{G}}_m = 0, \tag{2.59}$$

when there is no charge in the volume.

The two methods of solving dyadic Green's functions are derived either using the dyadic Green's function of the magnetic type, $\overline{\overline{G}}_m$, or of the electric type, $\overline{\overline{G}}_e$. The magnetic dyadic Green's function describes the magnetic field, while the electric dyadic Green's function describes the electric field. The magnetic dyadic Green's function of the second type, $\overline{\overline{G}}_{m2}$, uses the Ohm-Rayleigh method for finding the dyadic Green's functions [25, 29] and will be used in this work. Once the Green's function is acquired the magnetic field can be found by integrating Eqn. 2.55 over the source in Eqn. 2.53,

$$\overline{H}(x,y,z) = \int \overline{\overline{G}}_{m2}(x,y,z;x',y',z') \cdot \overline{M}(x',y',z'). \tag{2.60}$$

The resulting electric field can be found using $\boldsymbol{\nabla} \times \overline{H} = -i\omega\epsilon\overline{E}$.

In the following sub-sections, the use of dyadic Green's functions for two geometries will be derived: rectangular and cylindrical waveguides. In the derivation it will be assumed that the magnetic current source is known and lies on the wall of the waveguide. Once the dyadic Green's functions are found, discussion on the formulation of the magnetic current source using the equivalence principle is outlined.

2.2.6 Rectangular Waveguide Formulation

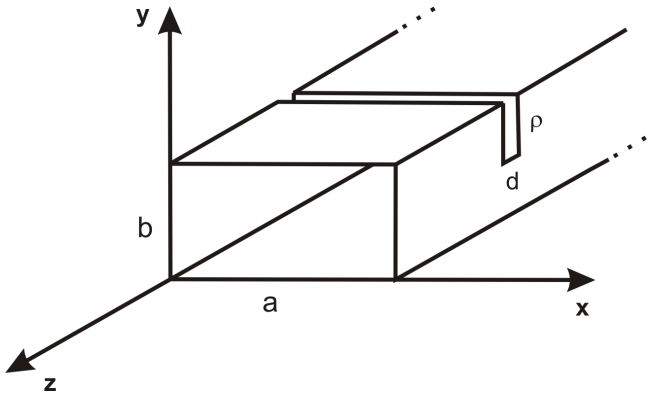

Figure 2.8: *Definition of the rectangular geometry with a slot thickness of* **d** *and a depth of* ρ *cut into the broad face of the waveguide. The walls of the waveguide are PEC material and have a cross-section of* **a** *by* **b**.

The rectangular waveguide is defined in Fig. 2.8, where $\hat{z}$ is the propagation vector

and the electromagnetic modes are bounded by $0 \leq x \leq a$ and $0 \leq y \leq b$. The vector wave equation is defined as

$$\nabla \times \nabla \times \overline{\Phi} - \kappa^2 \overline{\Phi} = 0, \tag{2.61}$$

where κ is arbitrary and Φ is an arbitrary eigenfunction that satisfies the Helmholtz wave equation. Since a rectilinear coordinate system is used, the Cartesian or rectilinear vector wave function is used:

$$\overline{\Phi} = \nabla \times (\psi_1 \hat{\mathbf{e}}), \tag{2.62}$$

where $\hat{\mathbf{e}}$ denotes a constant vector, $\hat{\mathbf{x}}$ $\hat{\mathbf{y}}$ or $\hat{\mathbf{z}}$, and ψ_1 is the characteristic function that satisfies the scalar wave equation

$$\nabla^2 \psi_1 + \kappa^2 \psi_1 = 0. \tag{2.63}$$

The function ψ_1 is known as the generating function, and $\hat{\mathbf{e}}$ is known as the piloting vector. It can be shown that Eqn. 2.62 is a solution of Eqn. 2.61 if ψ_1 is a solution for Eqn. 2.63. The set of functions obtained, denoted by $\overline{M}_\Phi$, is

$$\overline{M}_\Phi = \nabla \times (\psi_1 \hat{\mathbf{e}}). \tag{2.64}$$

Similarly, another set of equations, denoted by $\overline{N}_\Phi$, is described by

$$\overline{N}_\Phi = \frac{1}{\kappa} \nabla \times (\psi_2 \hat{\mathbf{e}}), \tag{2.65}$$

where ψ_2 does not have to equal ψ_1, but both must satisfy Eqn. 2.63.

Using the separation of variables method, the general solution to the scalar wave equation in rectangular coordinates can be written as

$$\psi = [A\cos(k_x x) + B\sin(k_y y)]\,[C\cos(k_y y) + D\sin(k_x x)]\,e^{ihz}, \tag{2.66}$$

where $k_x^2 + k_y^2 + h^2 = \kappa^2$. Since our geometry is a rectangular waveguide bounded by $0 \leq x \leq a$, $0 \leq y \leq b$ and $-\infty < z < \infty$ the boundary conditions can be defined. In

general, solutions that satisfy boundary conditions include

$$\begin{aligned} k_x &= \tfrac{m\pi}{a} \quad m = 0, 1, 2, 3, \ldots, \text{ and} \\ k_y &= \tfrac{n\pi}{b} \quad n = 0, 1, 2, 3, \ldots . \end{aligned} \tag{2.67}$$

The vector wave functions, both $\overline{M}_\Phi$ and $\overline{N}_\Phi$, satisfy the vector Dirichlet boundary conditions

$$\hat{\mathbf{n}} \times \overline{M}_\Phi = 0 \text{ and} \tag{2.68}$$

$$\hat{\mathbf{n}} \times \overline{N}_\Phi = 0 \tag{2.69}$$

on the waveguide walls.

Since the propagation direction, or piloting vector, is in the $\hat{\mathbf{z}}$ direction, $\hat{\mathbf{e}}$ is replaced by $\hat{\mathbf{z}}$. Then the complete $\overline{M}_\Phi$ and $\overline{N}_\Phi$ functions, which satisfy the vector Dirichlet condition, are

$$\overline{M}_{emn}(h) = \nabla \times [\psi_{emn}(h)\hat{\mathbf{z}}] = \nabla \times (\cos(k_x x)\cos(k_y y)e^{ihz}\hat{\mathbf{z}}) \text{ and} \tag{2.70}$$

$$\overline{N}_{omn}(h) = \frac{1}{\kappa}\nabla \times \nabla \times [\psi_{emn}(h)\hat{\mathbf{z}}] = \nabla \times \nabla \times (\sin(k_x x)\sin(k_y y)e^{ihz}\hat{\mathbf{z}}). \tag{2.71}$$

The subscript "o" is used to denote "odd," and the subscript "e", "even." It is understood that odd functions with m or n equal to zero are null modes. These modes are transverse magnetic modes and cannot have an m or n equal to zero. The vector functions that properly represent the magnetic field in a rectangular waveguide can be found by

$$\begin{aligned} \overline{M}_{omn}(h) &= \frac{1}{\kappa}\nabla \times \overline{N}_{omn} = (k_y \sin(k_x x)\cos(k_y y)\hat{\mathbf{x}} \\ &\quad - k_x \cos(k_x x)\sin(k_y y)\hat{\mathbf{y}})e^{ihz} \text{ and} \end{aligned} \tag{2.72}$$

$$\begin{aligned} \overline{N}_{emn}(h) &= \frac{1}{\kappa}\nabla \times \overline{M}_{emn} = \frac{1}{\kappa}(ihk_x \sin(k_x x)\cos(k_y y)\hat{\mathbf{x}} \\ &\quad - ihk_y \cos(k_x x)\sin(k_y y)\hat{\mathbf{y}} \\ &\quad + k_c^2 \cos(k_x x)\cos(k_y y)\hat{\mathbf{z}})e^{ihz}. \end{aligned} \tag{2.73}$$

The functions $\overline{M}_{omn}(h)$ and $\overline{N}_{emn}(h)$ satisfy the vector Neumann condition on the

boundary, mainly,

$$\hat{\mathbf{n}} \times \nabla \times \overline{M} = 0 \text{ and} \tag{2.74}$$

$$\hat{\mathbf{n}} \times \nabla \times \overline{N} = 0. \tag{2.75}$$

For this problem, the Neumann boundary condition are used for formulating the magnetic field solutions. From here, Tai [29, 25] notes the orthogonal properties of $\overline{M}_\Phi$ and $\overline{N}_\Phi$. Knowing the orthogonality properties of the vector wave functions, the functions are perpendicular so that integration over all solution space results in zero only during the conditions when $m \neq m'$ and $n \neq n'$.

Using the Ohm-Rayleigh method, the normalization factor is determined for the functions

$$\int_0^a \int_0^b \int_{-\infty}^{\infty} \overline{M}_{omn}(h) \cdot \overline{M}_{omn}(-h')dxdydz = \int_{-\infty}^{\infty} (1+\delta_0)\frac{\pi abk_c^2}{2}\delta(h-h')dz, \tag{2.76}$$

where the δ_0 function denotes the Kronecker delta functions, which is 1 if m or n is 0 and 0 otherwise. The null modes of $\overline{M}_{omn}(h)$ are included in this normalization since when m or n is zero, $\overline{M}_{omn}(h)$ has a normalization of zero. Similarly, the normalization of the $\overline{N}_{emn}$ function can be found by using

$$\int_0^a \int_0^b \int_{-\infty}^{\infty} \overline{N}_{emn}(h) \cdot \overline{N}_{emn}(-h')dxdydz. = \int_{-\infty}^{\infty} (1+\delta_0)\frac{\pi abk_c^2}{2}\delta(h-h')dz. \tag{2.77}$$

Once the vector wave functions are properly defined, the dyadic Green's function can be constructed. The eigenfunctions defined in $\overline{M}_\Phi$ and $\overline{N}_\Phi$ allow for the complete vector solution for the magnetic field in the waveguide.

The Method of $\overline{\overline{G}}_m$

The method of $\overline{\overline{G}}_m$ uses the Ohm-Rayleigh method to derive the magnetic dyadic Green's function of the second kind (Neumann boundary) for a rectangular waveguide using the vector wave equations. The dyadic Green's function, denoted $\overline{\overline{G}}_{m2}(\overline{r};\overline{r}')$, must satisfy the

equation

$$\nabla \times \nabla \times \overline{\overline{G}}_{m2}(\overline{r};\overline{r}') - k^2\overline{\overline{G}}_{m2}(\overline{r};\overline{r}') = \nabla \times \left[\overline{\overline{I}}\delta(\overline{r}-\overline{r}')\right] \text{ and} \tag{2.78}$$

$$\hat{\mathbf{n}} \times \nabla \times \overline{\overline{G}}_{m2}(\overline{r};\overline{r}') = 0. \tag{2.79}$$

Using the Ohm-Rayleigh method, an eigenvalue expansion is derived for the source function $\nabla \times \left[\overline{\overline{I}}\delta(\overline{r}-\overline{r}')\right]$ using the functions introduced earlier. For the magnetic field solutions and to satisfy the Neumann boundary conditions $\overline{N}_{emn}(h)$ and $\overline{M}_{omn}(h)$ are used. Expanding the source function using the vector wave functions yields

$$\nabla \times \left[\overline{\overline{I}}\delta(\overline{r}-\overline{r}')\right] = \int_{-\infty}^{\infty} dh \sum_{m=0}^{\infty}\sum_{n=0}^{\infty}\left[\overline{N}_{emn}(h)\overline{A}_{emn}(h) + \overline{M}_{omn}(h)\overline{B}_{omn}(h)\right], \tag{2.80}$$

where it can be shown that

$$\overline{A}_{emn}(h) = \frac{(2-\delta_0)\kappa}{\pi abk_c^2}\left(-\hat{\mathbf{n}}\cdot\left[\overline{N}_{emn}(h)\times\overline{\overline{I}}\delta(\overline{r}-\overline{r}')\right]\right) \text{ and} \tag{2.81}$$

$$\overline{B}_{omn}(h) = \frac{(2-\delta_0)\kappa}{\pi abk_c^2}\left(-\hat{\mathbf{n}}\cdot\left[\overline{M}_{omn}(h)\times\overline{\overline{I}}\delta(\overline{r}-\overline{r}')\right]\right). \tag{2.82}$$

Since the rectangular waveguide extends to infinity and since the integrand has two poles at $h = +/-(k^2-k_c^2)^{\frac{1}{2}}$, because k is complex, the solution meets the requirements of the Jordan lemma in the theory of complex variables [31]. Finally, the Green's function for the magnetic field satisfying the boundary condition of the second type can be shown as

$$\overline{\overline{G}}_{m2}(\overline{r};\overline{r}') = \frac{ik}{ab}\sum_{m=0}^{\infty}\sum_{n=0}^{\infty}\frac{(2-\delta_0)}{k_c^2k_g}\left[\overline{N}_{emn}(\pm k_g)\overline{A}'_{emn}(\mp k_g) + \overline{M}_{omn}(\pm k_g)\overline{B}'_{omn}(\mp k_g)\right], \tag{2.83}$$

where $z > z'$ corresponds to $\pm$ and $z < z'$ corresponds to $\mp$ for k_g and

$$\overline{A}'_{emn}(k_g) = -\hat{\mathbf{n}}\cdot\left[\overline{N}'_{emn}(\mp k_g)\times\overline{\overline{I}}\delta(\overline{r}-\overline{r}')\right], \text{ and} \tag{2.84}$$

$$\overline{B}'_{omn}(k_g) = -\hat{\mathbf{n}}\cdot\left[\overline{M}'_{omn(\mp k_g)}\times\overline{\overline{I}}\delta(\overline{r}-\overline{r}')\right]. \tag{2.85}$$

By integrating over the closed surface of the magnetic current source, $\overline{M}_s$, on the surface

of the waveguide walls such that

$$\overline{H}(x,y,z) = i\omega \int_S \overline{\overline{G}}_{m2}(x,y,z;x',y',z') \cdot \overline{M}_s(x',y',z')dS, \tag{2.86}$$

the solution to the magnetic field using $\overline{\overline{G}}_m$ is found. The volume integral of the Green's function vanishes because the excitation is on the waveguide walls.

The solution to Eqn. 2.86 is valid everywhere within the domain except at the source surface. In this work, Eqn. 2.86 is exclusively used to find the magnetic field in a rectangular waveguide. This derivation is necessary not only for full understanding of the solution, but also because previous derivations, in both Tai [29, 25] and Ho *et al.* [32], derive solutions for sources within the waveguide, not on the waveguide walls.

2.2.7 Cylindrical Waveguide Formulation

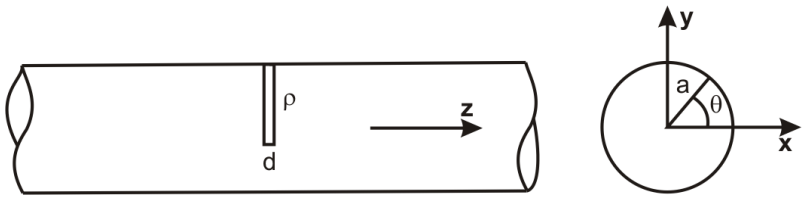

Figure 2.9: *Definition of the cylindrical geometry with a slot thickness of* **d** *and a depth of* ρ *cut into the broad face of the waveguide. The walls of the waveguide are PEC material and have a radius of* **a**.

Formulation of the cylindrical waveguide, depicted in Fig. 2.9 follows the same steps as the rectangular waveguide [29, 25]. In this case the characteristic equation uses cylindrical Bessel functions as the eigenfunction expansions. Again, the $\hat{z}$ is the propagation vector and the cylindrical modes are bounded by $0 \leq r \leq a$. The characteristic wave equation is then determined by

$$\psi_{\substack{e\\o}n\gamma'} = J_n(\frac{\gamma'_{mn}}{a}r)\,(\substack{\cos\\\sin}(n\phi))\,e^{ihz}\hat{z}, \text{ and} \tag{2.87}$$

$$\psi_{\substack{e\\o}n\gamma} = J_n(\frac{\gamma_{mn}}{a}r)\,(\substack{\cos\\\sin}(n\phi))\,e^{ihz}\hat{z}, \tag{2.88}$$

where, a is the radius of the cylindrical waveguide and γ_{mn} and γ'_{mn} are the zeros

associated with the Bessel function of the first kind or the derivative of the Bessel function of the first kind, respectively. The subscript 'e' denotes an even function where $\cos(n\phi)$ is used and the subscript 'o' denotes an odd function where $\sin(n\phi)$ is used. The wave constant for the two wave equations is defined as

$$k_\gamma^2 = \left(\frac{\gamma_m n}{a}\right)^2 + h^2, \text{ and} \tag{2.89}$$

$$k_{\gamma'}^2 = \left(\frac{\gamma'_m n}{a}\right)^2 + h^2. \tag{2.90}$$

Then the cylindrical vector wave functions can be defined by

$$\overline{M}_{\substack{e\\o}m\gamma'}(h) = \boldsymbol{\nabla} \times \psi_{\substack{e\\o}m\gamma'}, \text{ and} \tag{2.91}$$

$$\overline{N}_{\substack{e\\o}n\gamma}(h) = \frac{1}{k_\gamma}\boldsymbol{\nabla} \times \boldsymbol{\nabla} \times \psi_{\substack{e\\o}m\gamma'}, \tag{2.92}$$

where both satisfy vector Dirichlet boundary conditions at $r = a$. Using the Ohm-Rayleigh method and the method of $\overline{\overline{G}}_m$ as described in the previous section the dyadic Green's function for the cylindrical waveguide can be expressed as

$$\overline{\overline{G}}_{m2}(\overline{r};\overline{r}') = k\sum_{m=0}^{\infty}\sum_{n=0}^{\infty}\left[c_{\gamma'}\overline{N}_{\substack{e\\o}n\gamma'}(\pm k_{\gamma'})\overline{A}'_{\substack{e\\o}n\gamma'}(\mp k_{\gamma'}) + c_\gamma \overline{M}_{\substack{e\\o}n\gamma}(\pm k_\gamma)\overline{B}'_{\substack{e\\o}n\gamma}(\mp k_\gamma)\right], \tag{2.93}$$

where $z > z'$ corresponds to $\pm$ and $z < z'$ corresponds to $\mp$ for k_g and

$$\overline{A}'_{\substack{e\\o}n\gamma'}(k_{\gamma'}) = -\hat{\mathbf{n}} \cdot \left[\overline{M}_{\substack{e\\o}n\gamma'}(\mp k_{\gamma'}) \times \overline{\overline{I}}\delta(\overline{r} - \overline{r}')\right], \text{ and} \tag{2.94}$$

$$\overline{B}'_{\substack{e\\o}n\gamma}(k_\gamma) = -\hat{\mathbf{n}} \cdot \left[\overline{N}_{\substack{e\\o}n\gamma}(\mp k_\gamma) \times \overline{\overline{I}}\delta(\overline{r} - \overline{r}')\right]. \tag{2.95}$$

Additionally the constants $c_{\gamma'}$ and c_γ are defined as

$$c_{\gamma'} = \frac{i(2-\delta_0)}{4\pi\left(\frac{\gamma'}{a}\right)^2 k_{\gamma'} I_{\gamma'}}, \text{ and} \tag{2.96}$$

$$c_\gamma = \frac{i(2-\delta_0)}{4\pi\left(\frac{\gamma}{a}\right)^2 k_{\gamma'} I_\gamma}. \tag{2.97}$$

Finally, the scaling constants $I_{\gamma'}$ and I_{γ} are defined as

$$I_{\gamma'} = \frac{a^2}{2\left(\frac{\gamma'}{a}\right)^2}\left(\left(\frac{\gamma'}{a}\right)^2 - \frac{n^2}{a^2}\right) J_n^2\left[\left(\frac{\gamma'}{a}\right)^2 a\right], \text{ and} \tag{2.98}$$

$$I_{\gamma} = \frac{a^2}{2\left(\frac{\gamma}{a}\right)^2}\left[\frac{\partial J_n(\frac{\gamma}{a}r)}{\partial r}\right]^2_{r=a}. \tag{2.99}$$

Integrating the magnetic current source, $\overline{M}_s$, on the closed surface of the waveguide walls produces the solution,

$$\overline{H}(r,\phi,z) = i\omega \int_S \overline{\overline{G}}_{m2}(r,\phi,z;r',\phi',z') \cdot \overline{M}_s(r',\phi',z')dS. \tag{2.100}$$

2.2.8 Equivalence Principle

The previous sections provided the mathematical tools needed to construct a dyadic Green's function to solve a boundary-value problem of the Helmholtz wave equation in rectangular and cylindrical waveguides. In previous examples, that forcing function was arbitrary. In this section, the forcing function, or source, is derived using the surface equivalence principle.

The *surface equivalence principle* [24, 26, 33, 34, 35] is a mathematical technique that relates known sources to appropriate boundary conditions and equivalent sources. The equivalent sources are then used to solve the problem. The equivalence principle is useful in removing structures from the solution domain. For example, if a plane-wave in free space is incident on a PEC, shown in Fig. 2.10a, the scattered field can be calculated by using a magnetic current, shown in Fig. 2.10b, if the total electric field on the surface is known. The scattered fields of the original problem outside the PEC are equivalent to the scattered fields produced by the equivalent magnetic current.

In the formulation of the waveguide problem, an incident magnetic field, $\overline{H}_{inc}$, is applied outside the waveguide by a Helmholtz pair. It is assumed that the entire outside region of interest is excited uniformly. A slot cut into the side of the waveguide acts as the transmission between the outside and waveguide solution space. This slot becomes the source in the problem. In order for the Green's function to be valid, the physical slot must

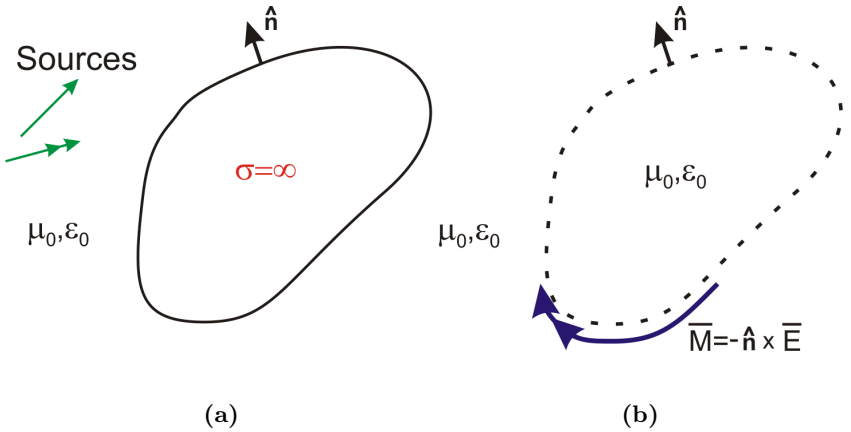

Figure 2.10: *The equivalence principle formulation on a PEC object. (a) The total electric field can be described as the addition of the incident and scattered wave off an object. (b) The object is replaced by an equivalent magnetic current source and all space is solved.*

be removed and replaced either by a magnetic or electric current with the equivalence principle.

It is assumed that the waveguide is PEC material. This has two benefits for the formulation of the problem: i) it can be assumed that the 100 kHz field applied outside the solution space is only transferred in through the predefined slot, and ii) it simplifies the equivalence principle by defining the source as only the magnetic current.

Single Slot Formulation

It is important to understand how the incident magnetic field reacts when it comes in contact with the outside of a PEC waveguide. To satisfy Maxwell's equations, the divergence of $\overline{B}$ must be zero. This is maintained by the ability of the magnetic flux to "bend" around the PEC waveguide, satisfying $\boldsymbol{\nabla} \cdot \overline{B} = 0$. An illustration of this "bending" is shown in Fig. 2.11a. This phenomenon is important to understanding how the eddy currents are formed on the surface of the waveguide. These currents can be described by

$$\overline{J}_s = \hat{\mathbf{n}} \times \overline{H}_{tot}, \tag{2.101}$$

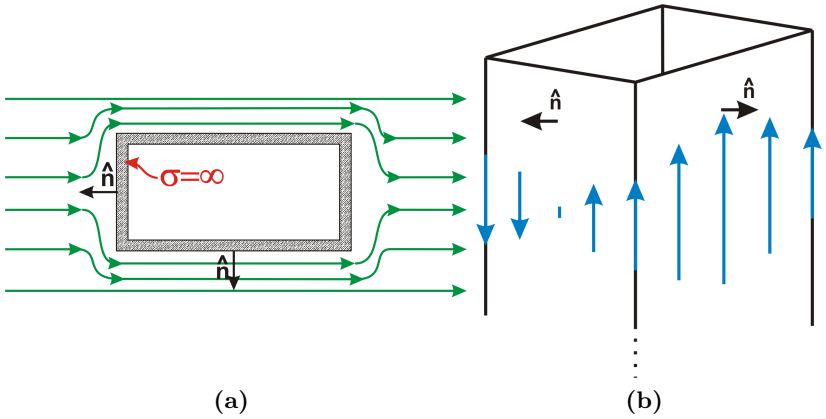

Figure 2.11: *Deviation of $\overline{B}$ around a PEC waveguide. (a) The magnetic field "bends" around the PEC waveguide. (b) By studying Eqn. 2.101, the eddy currents that are formed on the surface of the waveguide can be imagined.*

where $\hat{\mathbf{n}}$ is a normal vector facing out on the outer surface of the waveguide, illustrated in Figs. 2.11a and 2.11b.

Formulating the source for the waveguide problem is illustrated in Fig. 2.12. The incident magnetic field, $\overline{H}_{inc}$, is applied to the outside of the waveguide where an eddy current, $\overline{J}_e$, is formed on the outside surface by Faraday's law, shown in Fig. 2.12a. The eddy current produces two fields: i) a field anti-parallel to $\overline{H}_{inc}$, reducing the surface current on the face of the waveguide everywhere but at the edges, and ii) a field parallel to $\overline{H}_{inc}$ in the region of the slot. An electric field across the gap in the $\hat{\mathbf{z}}$ direction is also produced.

Using Eqn. 2.101 and studying Fig. 2.11a, the first step of the formulation of the slot sources using the equivalence principle can be better understood. The surface currents or *eddy currents* can be envisioned by following the lines of flux illustrated in Fig. 2.11b. The electric field inside the cut slot is the result of these surface currents. The slot thickness, d, and slot depth, a, are the two variables used to create the magnitude and shape of the electric field in the gap, primarily $E\hat{\mathbf{z}}$, illustrated in Fig. 2.13a. Boundary conditions require that $E_{tan}\hat{\mathbf{z}} = 0$ on the surface. This requirement produces a half-sinusoidal shape around the circumferential slot length, with zero on the depth face, shown in Fig. 2.13b. The electric field magnitude and direction are characterized using

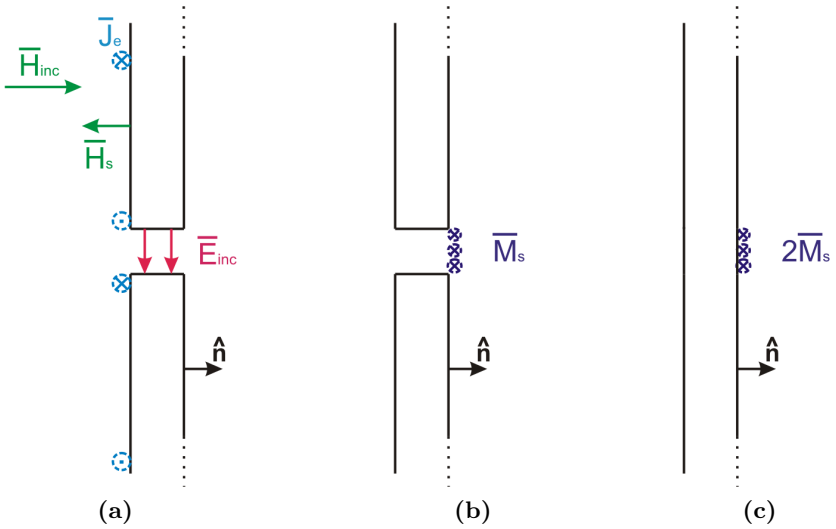

Figure 2.12: *Formulation of slot sources on a PEC waveguide using equivalence principle. (a) Incident magnetic field, $\overline{H}_{inc}$, creates an eddy current on the surface of the waveguide, $\overline{J}_s$. The eddy current creates a scattered magnetic field, $\overline{H}_s$, and the potential across the gap creates an incident electric field, $\overline{E}_{inc}$. (b) The electric field is then replaced by a magnetic current, $\overline{M}_s$, using Eqn. 2.102. (c) Using image theory, the slot is removed and is replaced by an equivalent magnetic surface current.*

Ansoft HFSS simulations. The field profile and amplitude is used in the calculation of the magnetic current source.

Since the wavelength of this problem is much greater than the size of the slot and the material is PEC, it is assumed that there is no attenuation or phase differences in the transmission of the electric field from the outside to the inside of the waveguide. This assumption allows for the exchange of the electric field in the slot to a magnetic current on the inside surface of the waveguide, defined by

$$\overline{M}_s = -\hat{\mathbf{n}} \times E\hat{\mathbf{z}}, \tag{2.102}$$

where $\hat{\mathbf{n}}$ is a normal vector facing into the waveguide, as shown in Fig. 2.12b). Finally, the equivalent source can be found by using image theory. With image theory, the entire slot is replaced by a waveguide wall with a magnetic current source on the surface, as shown in Fig. 2.12c. The process is repeated for all sides of the waveguide that are cut by the slot.

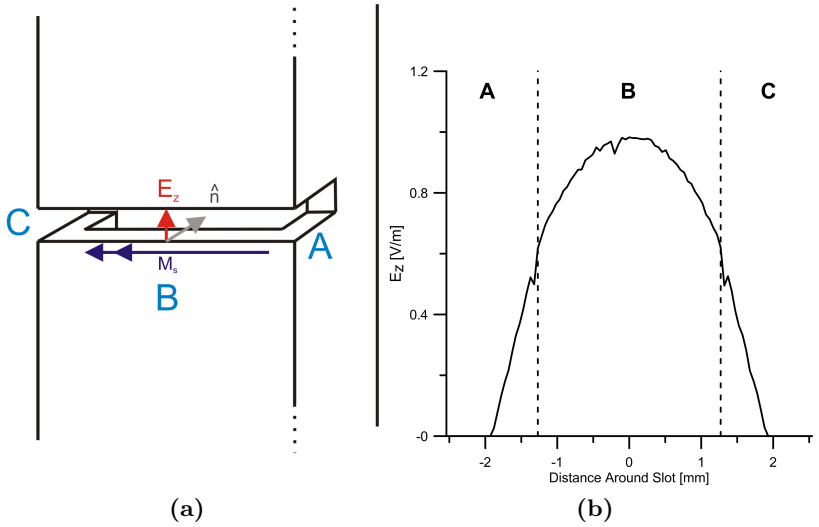

Figure 2.13: *Formulation of the Magnetic Current using $E_z\hat{z}$. The surface magnetic current, $\overline{M}_s$ is derived from the (a) electric field potential within the slot. (b) The formulation of electric field creates a cosine like amplitude around the slot, the dashed lines represent the corners of the internal wall of the waveguide.*

The assumption that the magnetic current is only located on the surface area of the slot is known as Born's first approximation, Ref. [33]. *Born's first approximation* is described as:

> [...] if the wave is expressed as the sum of the incident wave and a diffracted wave secondary wave, the scattering of the secondary wave is neglected. This represents what is usually known as Born's first approximation, and finds many applications in the theory of scattering of X-rays and electrons.

Visually, Born's first approximation can be illustrated using Fig. 2.14a. Here, the blue dashed lines represent the walls of a slot cut into PEC material. If the wavelength is much smaller than the slot, the field in the slot can be estimated by a unit step function. The "secondary wave" on the outsides of the slot boundary can be ignored. However, if the wavelength is much larger than the slot, as illustrated in Fig. 2.14b, the secondary wave can be comparable in field density to the primary wave inside the slot boundaries. Thus, Born's first approximation is not valid for this problem, and the secondary wave effect must be accounted for in the characterization of the magnetic current. This problem

can be described as near-field diffraction of evanescent and propagating waves [36] which result from boundary conditions within the slot.

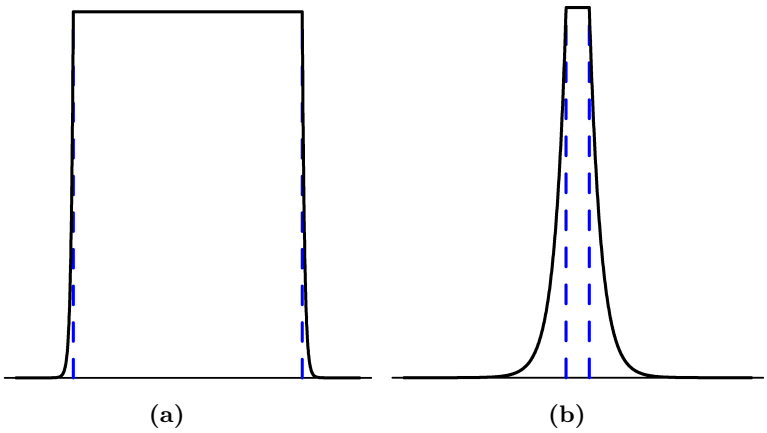

Figure 2.14: *Wavelength variations of Born's first approximation in a cut slot. The slot boundary is represented by the two blue dashed lines, while the field approximation is illustrated by solid black lines. (a) If the wavelength, λ, is much smaller than the slot thickness the secondary wave can be ignored. (b) However, if the wavelength is much much larger than the slot thickness, the two fields inside and outside the slot boundary are comparable.*

Characterization of the surface magnetic current source is illustrated in Fig. 2.15. Using a unit step function the width of the cut slot as predicted by Born's first approximation, shown as a dashed orange line, was found to be inadequate due to the secondary wave. It was found that creating a unit step function 2.5 times larger than the slot width, shown as a solid purple line, was needed to produce adequate results. However, a surface magnetic current in the shape of a unit function does not make physical sense. Therefore, in the formulation of the source, a Gaussian shaped surface magnetic current, $\overline{M}_s$, was characterized, as illustrated in Fig. 2.15 dashed black lines.

Using a Gaussian shape gives physical insight to the distribution of the electric field and, therefore, the surface magnetic current source from the slot. Since the distribution of the surface magnetic current source is more complicated than a simple unit step function, the equivalent surface magnetic current is replaced with a single magnetic current filament source, $\overline{M}_f$, located on the surface of the waveguide walls along the center of the slot. The solution to the problem is then solved by performing a posterior

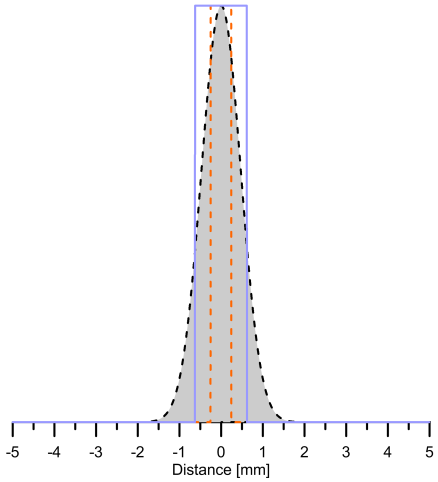

Figure 2.15: *Characterization of magnetic surface current source. A unit step function is used as the surface magnetic current which fills the exact slot thickness (orange dashed) as predicted by Born's first approximation. To minimize error, the unit step function was made wider than the actual slot (purple). However, surface magnetic current actually has a Gaussian shape (black dashed) that extends past the slot thickness.*

product (Eq. A-6) of the surface magnetic current filament and Eqn. 2.86 for a rectangular waveguide, and, likewise, using Eqn. 2.100 for a cylindrical waveguide. To account for the distribution of magnetic current, the convolution of the solution with a properly characterized Gaussian function, such as one described in Fig. 2.15, is used to describe the primary and secondary waves associated with the slot. Using convolution, a complete solution can be formed.

2.3 Computational Methods

With the progression of computer technology to multi-core processors, it has become increasingly efficient to use computer simulation models to test experimental ideas. Through these virtual experiments, one can gain intuition and refine theory to better describe the models. With symmetric geometries, closed-form solutions of boundary-value problems are solved using a variety of methods such as Green's functions or vector potential solutions. This solution space either is represented by a modal solution or a total field solution. With a modal solution, orthonormal basis functions are summed together to

form the solution, while total field solutions use a direct method to describe the fields in the solution.

While analytical methods have laid the groundwork for theoretical advancement, practical solution space is not always solvable in a closed-form solution. To solve these problems, numerical methods are used. Many numerical methods have been developed such as the finite-difference time-domain (FD-TD), the finite-element method (FEM), and the method of moments (MoM). Each method has its strengths and weaknesses and is valid for many different boundary-value problems. Here, the focus will be on finite-element modeling using two commercially available FEM programs: Ansoft (Pittsburgh, PA) High Frequency Structure Simulator (HFSS; version 12.0) and Ansoft Maxwell 3D (version 12.0).

Maxwell 3D uses a quasi-static approach to solve Maxwell's equations. In general this means that spatial phase differences in the geometry are not calculated. Maxwell 3D is very useful for eddy current problems and calculations of ohmic heating due to low-frequency electromagnetic waves. Ansoft HFSS is a full-wave finite-element modeling program. It uses no known approximations to solve Maxwell's equations on a given boundary.

2.3.1 Finite-Element Method

The finite-element method developed as a way to solve complex structural analysis problems and can be traced back to Alexander Hrennikoff [37] and Richard Courant [38]. Both developers created a discretization of a continuous domain by creating a mesh of sub-domain elements. The solution is then solved on the sub-domains and later extrapolated to the whole domain. The method by Richard Courant, where finite triangular subregions are used to solve partial differential equations (PDE), is more widely used. A more detailed history can be found in Refs. [39], [40], and [41].

As an example, a two-dimensional object is created as a solvable domain, as shown in Fig. 2.16a. The domain is then split into an arbitrary number of sub-domains by way of meshing (Fig. 2.16b). The trade-off in the finite-element method is between the number of sub-domains and the total error of the solution. As the number of sub-domains increase,

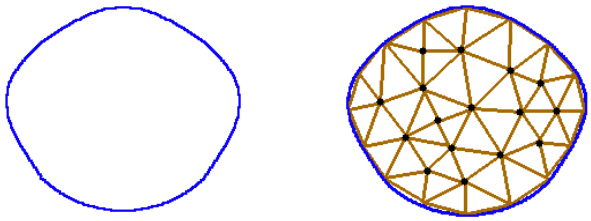

(a) **(b)**

Figure 2.16: *A two-dimensional finite-element method takes an arbitrary domain (A) and breaks it into sub-domains (B) using a mesh. This mesh becomes a numerical representation of the object; error in the solution arises from approximations on the surfaces.*

the number of unknowns increase, using more memory and CPU time to formulate and solve the solution matrix. With too few sub-domains, the irregular object would not have an adequate approximation to its actual shape.

Each sub-domain is connected via its vertices, and each connection is called a *node*. Each node is assigned a number, and a connectivity array is created describing the interlacing of the sub-domains to each other. Nodes are either described as *open* or *fixed*. An open node represents a node that requires a solution, while a fixed node represents either a boundary value or source value. In the case of Fig. 2.16b, all of the vertices that are attached to the geometry boundary would be considered fixed nodes. In the formulation of the problem, these nodes would either be set with Neumann or Dirichlet boundary conditions or source values, depending on the application of the problem.

Once the domain is discretized, the unknown function, $\phi(x, y)$, must be approximated for each element. In the case of linear triangles, the unknown function can be described as a linear system, as shown in Eqn. 2.103,

$$\phi(x, y)^e = a^e + b^e x + c^e y, \tag{2.103}$$

where a^e, b^e, and c^e are constants that need to be determined for each sub-domain element, e. With each sub-domain function, a collection of linear equations can be assembled.

Both an elemental matrix and complete domain matrix are compiled using the unknown function, $\phi(x, y)$. Either a boundary formula or a variational formula can be applied. The variational formula is a mathematically derived integral that describes the system by finding the lowest energy value in an energy function. The boundary formula uses the boundary conditions and PDE of the system to formulate the solution. Both formulations have advantages and disadvantages.

Two solution spaces exist in finite-element analysis: *driven mode* and *eigenmode*. In a generalized eigenmode solution, the linear system of equations takes the form

$$[A]\,[\phi] - \lambda\,[B]\,[\phi] = 0, \tag{2.104}$$

where $[A]$ and $[B]$ are known matrixes and $[\phi]$ and λ are unknowns. In the solution to an eigenmode problem, the eigenvalue, λ, is solved directly. For every eigenvalue, a unique set of eigenvectors, $[\phi]$, exists. No sources or forcing functions are needed; all of the information of the boundaries and domains is found in $[A]$ and $[\phi]$.

Driven mode is the solution of the domain where a source or forcing function is present in the problem. A generalized driven mode solution takes the form

$$[A]\,[\phi] = [b]\,, \tag{2.105}$$

where $[A]$ is a known matrix, $[b]$ is a known set of sources, and $[\phi]$ is an unknown vector.

The finite-element method is general enough to be used on any set of partial differential equations. For electromagnetics, the set of PDEs used in the finite-element method is Maxwell's equations. Maxwell's equations describe the relationship between electric and magnetic fields and relate them to their sources. Complex medium and geometries can be described using some form of Maxwell's equations. For more information about finite-element method formulations and uses in electromagnetics see Ref. [42].

Many laboratories have attempted to produce home-built, finite-element method codes for solving specific problems, but they typically fail as a general method. Over the last ten years, commercial software firms such as Ansoft have developed a full suite of

tools to draw, define, and excite three-dimensional objects, which are automatically discretized and the electromagnetic solution using a formulation of Maxwell's equations is found. Additionally, a collection of post-processing tools has been added to the suite for viewing solutions and calculating additional information from the solution.

2.4 Methods

This work relies on both analytical and numerical solutions. The dyadic Green's functions are derived using a number of references cited in this work and are solved analytically by programming them into Wolfram (Champaign-Urbana, IL) Mathematica (version 7.0.2). The newest Mathematica includes pre-defined parallel programming functions such as *ParallelSum* and *ParallelTable*, using these new functions solutions to the dyadic Green's functions were accelerated by 76% resulting in solution times of approximately 8 minutes from 30 minutes.

Some discrepancies in surface currents were found between Maxwell 3D and HFSS that were not expected in the solution. This discrepancy is illustrated in Fig. 2.17. A box was drawn and a slot was cut into the side. In the Maxwell 3D solution, shown as the dashed lines, the current is formed on the surface along the top and is zero on the bottom of the slot. In the HFSS solution, shown as the solid line, the current follows positive on the top and negative on the bottom creating the proper potential to allow penetration of the magnetic field. It is also interesting to see that the HFSS solutions are continuous, while the Maxwell 3D current patterns are irregular. It is postulated that assumptions made in Maxwell 3D on the surface, due to the quasi-static simplification, were the cause of the differences. Solutions were found to be accurate within the waveguide in both programs, but since this work focuses on understanding the current patterns and how they couple into the waveguide, HFSS was chosen as the numerical solutions program.

Parameters such as the electric field amplitude and profile within the slot are taken from Ansoft HFSS solutions and used in the formulation of the dyadic Green's functions. This ensures that the dyadic Green's functions and HFSS solutions are comparable.

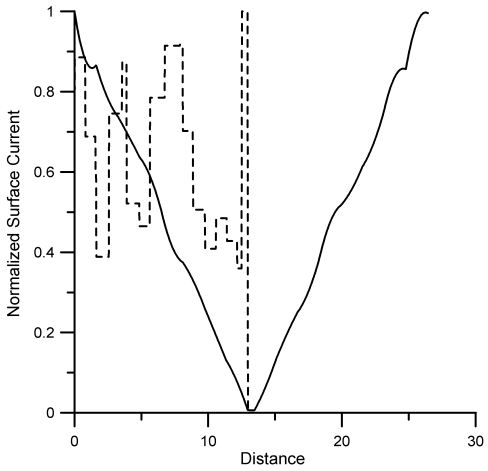

Figure 2.17: *Comparison of Ansoft Maxwell 3D and HFSS. The Maxwell 3D quasi-static solution (dashed) has an improbable current distribution, where the HFSS full-wave solver solid as a continuous current around the cut slot.*

2.4.1 Results and Discussions

Once all solutions are formed, the analytic and numerical solutions are compared using both visual and analytical techniques. Visually, a two dimensional cross-section solution of the solved waveguide are plotted in a side-by-side comparison to view contour similarities. If reasonable agreement is found between the analytical and numerical solutions, then the proper electromagnetic modes and their coefficients are assumed.

Since this work focuses on an axial uniform 100 kHz magnetic field, one must ensure the evanescent roll-off and field amplitude profile are properly reflected in the dyadic Green's function. A root-mean-square error function was employed to calculate the error between the normalized analytical and numerical results. Both equations are discretized into n segments and directly compared according to

$$\text{RMSE} = \sqrt{\frac{1}{n}\sum_{m=1}^{n}(H_{cal} - H_{sim})^2}. \tag{2.106}$$

Both the visual and analytical analysis gives confidence in dyadic Green's functions solution and the resulting insight and discussion of this work's results. It should be noted that the RMSE calculation in Eqn. 2.106 is not a percentage. Instead the RMSE measures individual differences, or residuals,from the control and in this form is a good measure of

precision.

In order to minimize Mathematica calculation time, the number of modes that are solved in the analytical code was varied until the solutions had an acceptable convergence. It was found that using ten TE and nine TM evanescent modes resulted in more than adequate convergence. These results were consistent in rectangular and cylindrical waveguides.

Chapter 3: Results

Surface currents arise when a time-varying electromagnetic field is incident on a conductor. These surface currents, or *eddy currents*, create a magnetic field that opposes the incident field[43]. In a problem where a hollow conducting object is electrically thick, no fields penetrate into the conductor center. In order for significant electromagnetic fields to defuse into a hollow object, slots are cut perpendicular to the object's axis.

Using numerical and analytical techniques, the physics that defines how the incident electromagnetic time-varying field penetrates into the hollow conducting object can be understood and visualized. Ansoft HFSS is an accurate tool for solving an electromagnetic problem, but it provides no real understanding of the physics behind the solution. The advantage of using dyadic Green's functions is that the formulation of the modes and sources provides a new level of understanding to the problem. In solving dyadic Green's functions, careful analysis of the source functions must be performed to ensure proper results. In the previous sections, the magnetic source is within the domain and can be calculated from the electric field from Eqn. 2.102. To form the dyadic Green's function a total of ten TE modes and nine TM modes are used to formulate the solution.

In Section 3.1, the eddy currents outside the waveguide domain will be analyzed in order to better understand the formulation of the sources. From this understanding, Section 3.2 describes the integration of the dyadic Green's function and proper source shapes. The solutions to a rectangular and cylindrical hollow cross-section are presented in Sections 3.3 and 3.4, respectively.

3.1 Single Slot Eddy Current Analysis

There are a variety of ways to solve and formulate an eddy current problem on a conducting finite plane [44, 45]. In this work, Ansoft HFSS was used as a tool to characterize the eddy currents outside the waveguide domain and better understand the formulation of the sources for the dyadic Green's functions.

In this example, a finite PEC plate is placed in the xy-plane and excited with an incident magnetic field in the -$\hat{z}$-direction oscillating at 100 kHz. Similar to Fig. 2.11a, the

magnetic flux must "bend" around the finite PEC plate. By visualizing Eqn. 2.101, the resultant surface current concentrates mainly along the edges of the plate, shown in Fig. 3.1a. The surface currents produce a scattered magnetic field, H_s, that opposes the incident magnetic field, H_{inc}

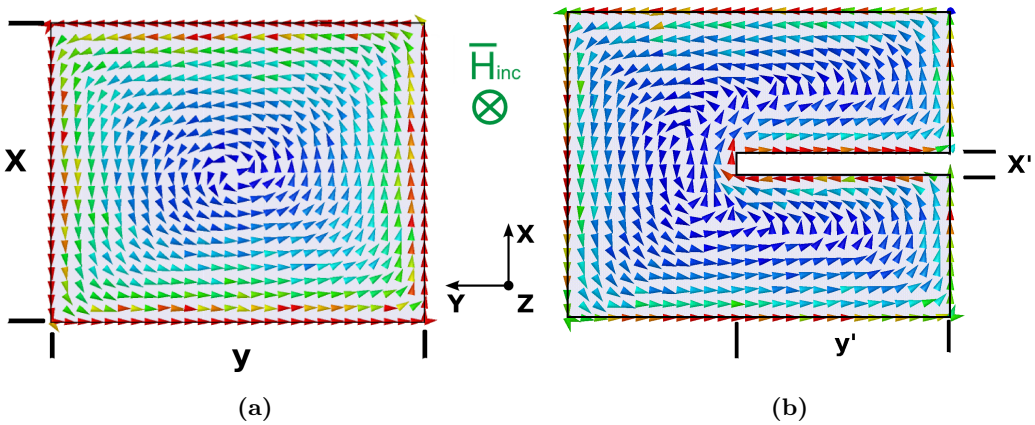

Figure 3.1: *Eddy current analysis on a finite PEC plate using Ansoft HFSS. The incident magnetic field is orientated in the -z-direction. Solutions are comparable to Fig. 3.2, which gives insight to eddy current patterns using Eqn. 3.1.*

When a slot is cut into the plate, shown in Fig. 3.1b, the surface currents induced "flow" around the edges. By using the curl of the incident magnetic field, the surface currents on the plate can be visualized. The surface currents on the plate surface induce a scattered magnetic field that opposes the incident magnetic field. However, the surface currents around the slot edges inside the gap add to the incident magnetic field forming a field that penetrates into the hollow conductor.

The eddy current problem can be viewed analytically from the total magnetic field, H_{tot}, comprised of the incident magnetic field, $\overline{H}_{inc}$, and opposing scattering magnetic field, $\overline{H}_s$. From Ref. [46], the analytical solution for the total magnetic field on a finite plate with uniform incident magnetic field can be expressed as

$$\overline{H}_{tot}(x,y,t) = H_{inc}\frac{16}{\pi^2}\sum_{n=0}^{\infty}\sum_{m=0}^{\infty} C_{nm}\cos\left(P_n x\right)\cos\left(Q_n y\right)e^{-\lambda_{nm}^2 t}\hat{z} - H_{inc}\hat{z}, \qquad (3.1)$$

where

$$C_{nm} = \frac{(-1)^{m+n}}{(2n-1)(2m-1)}, \tag{3.2}$$

$$P_n = \frac{2n-1}{2a}, \tag{3.3}$$

$$Q_m = \frac{2m-1}{2b}, \text{ and} \tag{3.4}$$

$$\lambda_{nm} = \sqrt{\frac{P_n^2 + Q_n^2}{\mu\sigma}}. \tag{3.5}$$

Equation 3.1 can be viewed as an eigenmode expansion of the magnetic fields on the surface of the conductor.

Note that a surface current is related to the electric field by the electric conductivity, $\overline{J}_e = \sigma\overline{E}_s$. Thus, the eddy currents can be shown to be proportional to the curl of the magnetic field of Eqn. 3.1. Since it is assumed that all conductors are PEC material, the eddy current is only formed on the surface of the conductor, resulting in $\overline{J}_e$ outside the waveguide domain.

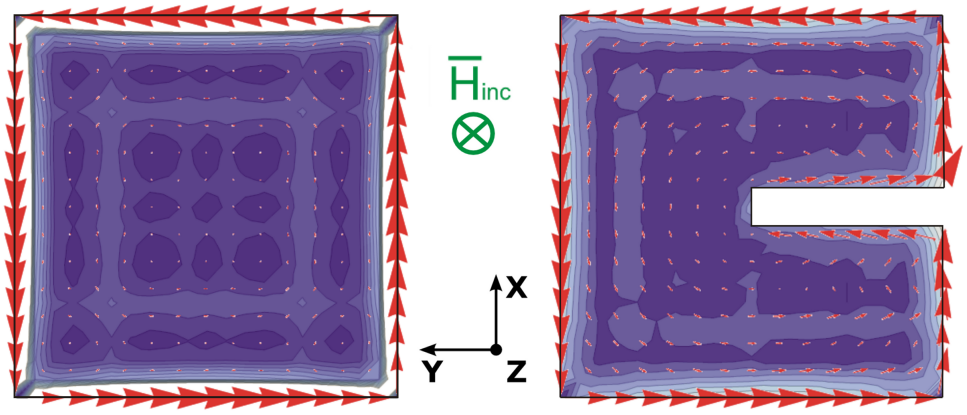

(a) **(b)**

Figure 3.2: *Eddy current analysis on a finite plate using the curl of Eqn. 3.1. The incident magnetic field is orientated -$\hat{z}$-direction.*

The approximation using Eqn. 3.1 is confirmed by visual inspection where a comparison between Ansoft HFSS and analytical results are shown, Figs. 3.2 and 3.1 respectively. Here a uniform incident magnetic field is applied -$\hat{z}$-direction, resulting in the

surface current vectors shown in both sub-figures. The advantage of using Eqn. 3.1 is the additional visualization of the mechanisms involved in the formulation of the eddy currents. It is clear from the equation, that the total magnetic field is comprised of an uniform incident magnetic field and an eigenmode expansion of an opposing scattering magnetic field.

When a single slot is cut in the plate the surface currents follow the boundary around the slot, shown in Fig. 3.2b. By including another scattering term in Eqn. 3.1, the effect of the slot on the plate can be included. The second scattering term is added to the incident magnetic field, such that

$$\overline{H}_{tot}(x,y,t) = H_{scat}(x,y)\hat{z} - \left[H_{inc}\hat{z} + H_{scat}(x',y')\hat{z}\right], \tag{3.6}$$

where x' and y' are the dimensions of the slot and H_{scat} is the eigenmode expansion of the magnetic field described in Eqn. 3.1.

From this analysis one can imagine a slot having current of equal but opposite magnitude on the top and bottom of the slot boundary. This configuration creates a potential giving rise to an electric field in the $\hat{x}$-direction. It has been shown in Ansoft simulations and by boundary condition analysis, that the electric field is strictly zero at the slot wall parallel with the x-axis. The electric field in the $\hat{x}$-direction rises sinusoidally in the negative $\hat{y}$-direction. From inspecting Fig. 2.11a and Eqn. 2.101, the electric field continues in a sinusoidal fashion in the negative $\hat{z}$-direction to the middle of the waveguide. These results are confirmed using Ansoft HFSS, shown in Fig. 2.13. The same analysis is tested and confirmed for the cylindrical case using Ansoft HFSS.

Propagation into the Domain

Typically in the understanding of eddy currents, the time-varying electromagnetic field is assumed to be quasi-static. This means that the displacement current, $\partial D/\partial t$, is negligible [43, 44, 45, 46]. In the case of a quasi-static approximation, the Helmholtz equation reduces to the Laplace equation, where the solutions are evanescent diffusion waves.

Since the wavelength of the time-varying electromagnetic field is significantly

larger than the slot depth, and the losses due to a high conductivity or PEC material are negligible, the potential created by the eddy currents on the outside of the domain directly transfer into the waveguide domain without any degradation. This potential across the slot gives rise to $\overline{E}_{inc}$, which is defined as $E_z\hat{z}$. From here, the equivalence principle is used to remove the physical slot from the solution space and replace it with a magnetic current inside the domain, as outlined in Section 2.2.8.

3.2 Integration of the Source

In order to properly form the analytical solution, the integral of the magnetic surface current source was broken up into two steps. The first step is to solve a Riemann sum of a magnetic current filament, $\overline{M}_f$, along the center of the slot path. The discretized delta source filament is then convolved with a source profile, M_{conv}, in order to create a 2.5-dimensional[1] source to be used in the formulation of the solution.

A *Riemann sum* is a computational technique where an integration is approximated by a number of discretized segments [47], such that

$$\int_0^a g(x)dx \cong \frac{1}{N}\sum_{n=0}^{N} g\left(\frac{na}{N}\right). \tag{3.7}$$

The discretization of the current filament produced more accurate results than Mathematica's built-in numerical integration technique. It is hypothesized that the small features of the slot, compared to a wavelength, created a challenge for the built in numerical integration. Using the Riemann sum technique, the step size was varied until results with low RMSE values were realized.

In the definition of the source function, the filament is placed along the center of the slot area and has the profile depicted by Eqn. 2.102 and Fig. 2.13a. The profile extends from one edge of the slot and follows the circumference of the waveguide along the slot center. The source profile is then used in the posterior scalar dot product with the

[1]The term *2.5-dimensional* is defined as a two-dimensional area that spans multiple normals. In this case, the waveguide has two normal vectors in the $\pm\hat{x}$-direction and one in the $-\hat{y}$-direction. Resulting in three combined two-dimensional areas with multiple normal vectors. This is why $\overline{M}_f$ is a vector, and M_{conv} is a scalar.

dyadic Green's function as expressed in Eqns. 2.86 and 2.100 for the rectangular and cylindrical waveguide, respectively.

The solution to the first step is two evanescent modes decaying in the $\pm\hat{z}$-direction centered at the source, shown in Fig. 3.3a (solid black). This solution has all of the evanescent information due to the superposition of the coupled modes for a single infinitesimal magnetic surface current filament, $\overline{M}_f$.

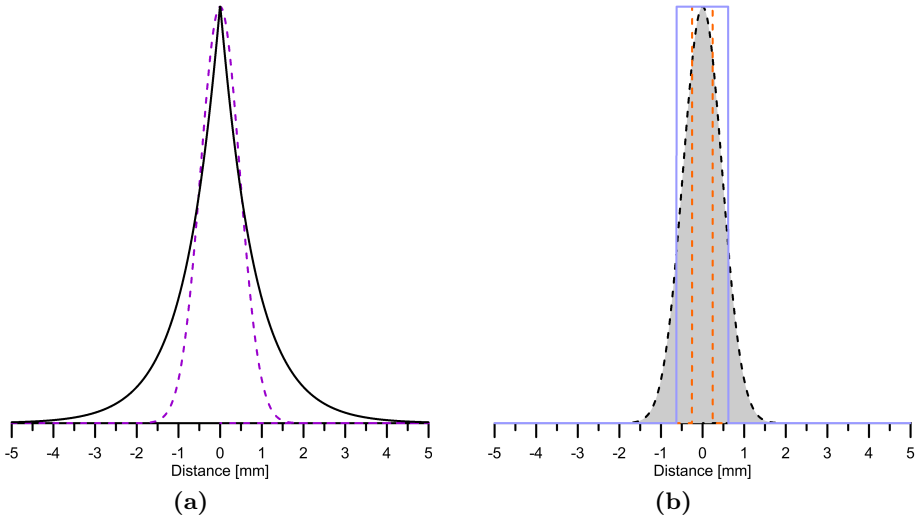

Figure 3.3: *(a) Normalized magnetic field solution along the axis of the rectangular waveguide using $\overline{M}_f$ (black) and convolution technique to account for slot thickness and near field effects (purple dashed). (b) Characterization of magnetic surface current source used in convolution solution. Using a unit step function the slot thickness (orange dashed). A unit step function 2.5x wider than the actual slot (purple). Gaussian shape (black dashed) profile.*

The first result using a unit step function with thickness d for M_{conv}, as described by Born's first approximation, was found to not adequately represent the actual current profile within the waveguide and resulted in a large RMSE.

As described in section 2.2.8, the assumption that the surface magnetic current source is a unit step function with the slot thickness, M_{conv} profile shown in Fig. 3.3b as an orange dashed line, is not appropriate for a slot significantly smaller than a wavelength. Results using an over compensating unit step function 2.5 times the size of the slot width, $2.5d$, resulted in a smaller RMSE, M_{conv} profile shown as a purple line in Fig. 3.3b.

The low RMSE error for an oversized profile is consistent with the hypothesis that

the Born's first approximation is not appropriate and that the incident field and near field effects around the slot are comparable in amplitude as the magnetic current within the slot, as illustrated in Fig. 2.14b.

Although increasing a unit step function to $2.5d$ resulted in a smaller RMSE, it is not accurate to describe near field effects as a unit step function. Instead, a Gaussian shape is more natural for near field diffusion waves. Using Ansoft HFSS to characterize the magnetic surface current the Gaussian profile was confirmed. The 2.5-dimensional discretized convolution is then described as

$$M_s = \sum_{n=-500}^{500} \overline{M}_f(n) \otimes M_{conv}(n), \tag{3.8}$$

where

$$M_{conv} = e^{\frac{-z^2}{2\sigma^2}}. \tag{3.9}$$

Here, σ is the standard deviation, or width, of the Gaussian function. Using a magnetic current convolution profile of a Gaussian function in Eqn. 3.8 results in a very small RMSE for both rectangular and cylindrical solutions. In Eqns. 3.9, the standard deviation of the Gaussian, σ, is 0.0797 for the rectangular waveguide and 0.1335 for the cylindrical waveguide. This deviation is measured in millimeters and can be compared to the actual slot depth of 0.05 mm. This result is important to understanding the deviation from Born's first approximation by adding the effect of a secondary wave, illustrated in Fig. 2.14b.

3.3 Single Slot Rectangular Results

The rectangular geometry used for the formulation of the solution is illustrated in Fig. 3.4. The lowest order mode in the rectangular waveguide with the dimensions 2.54 $\times$ 1.27 mm is the TE_{10} with a cut-off frequency of 59.055 GHz, which makes 100 kHz well below propagation cut-off. The propagation of all modes coupling into the waveguide are then evanescent.

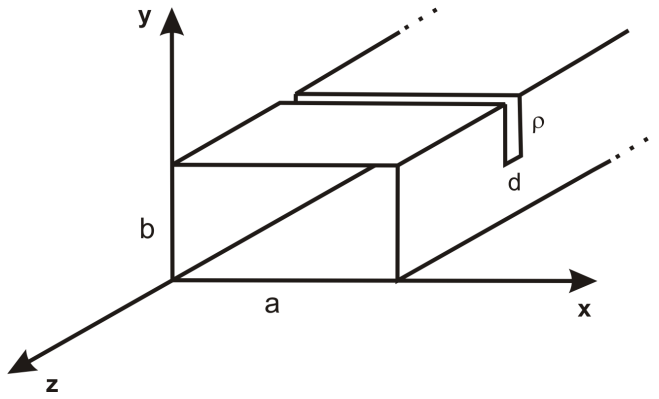

Figure 3.4: *Rectangular geometry used for a single slot. Where b is 1.27 mm and a is 2.54 mm. The center of the slot is located on the xy-plane with a depth, ρ, of 0.635 mm and a thickness, d, of 0.05 mm.*

A two-dimensional contour plot of the evanescent mode solutions using the dyadic Green's functions and the convolution techniques described in Section 3.2, are shown in Fig. 3.5. The contour plots are of the normalized magnetic field magnitude (H_{abs} shown in Fig. 3.5a) and the individual vector components: H_x, H_y, and H_z; Figures 3.5b, 3.5c, 3.5d, respectively. The slot source was a single slot cut into the right face of the waveguide in the $\hat{y}$-direction with a slot thickness, d, of 0.05 mm. For the initial results the slot depth was half the waveguide thickness, ρ is 0.625 mm. The slot cut is indicated in all figures as a black outline. The applied magnetic field is uniform and in the $\hat{x}$-direction. In this calculation the number of modes used were ten TE modes and nine TM modes.

The results are visually compared to Ansoft HFSS data, shown in Fig. 3.6. Good agreement between analytical and numerical results are shown. The results from the dyadic Green's functions show a slightly larger gradient of magnetic field in the $\hat{y}$-direction.

Since it is only the components parallel to the static magnetic field that create the field modulation effect, the most important component for EPR signal integrity is the $\hat{x}$-component. It is interesting to note in Fig. 3.5b, that the H_x component of the magnetic field does not have a uniform cross-section. If a sample of some arbitrary thickness was to be placed down the axis of the rectangular microwave cavity, it is clear that the differential field modulation amplitude would vary in both $\hat{x}$ and $\hat{y}$ directions,

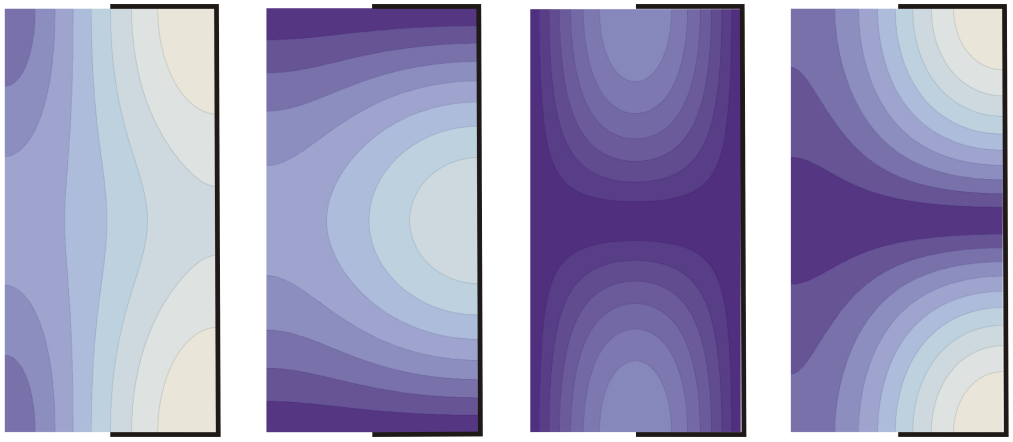

Figure 3.5: *Rectangular Waveguide Solutions using dyadic Green's functions. Slot cut 50% deep from right side. The magnetic field profile components are (a) magnetic field magnitude, (b) $\hat{x}$-component, H_x, (c) $\hat{y}$-component, H_y, (d)$\hat{z}$-component, H_z. Each contour represents a 10% change in amplitude.*

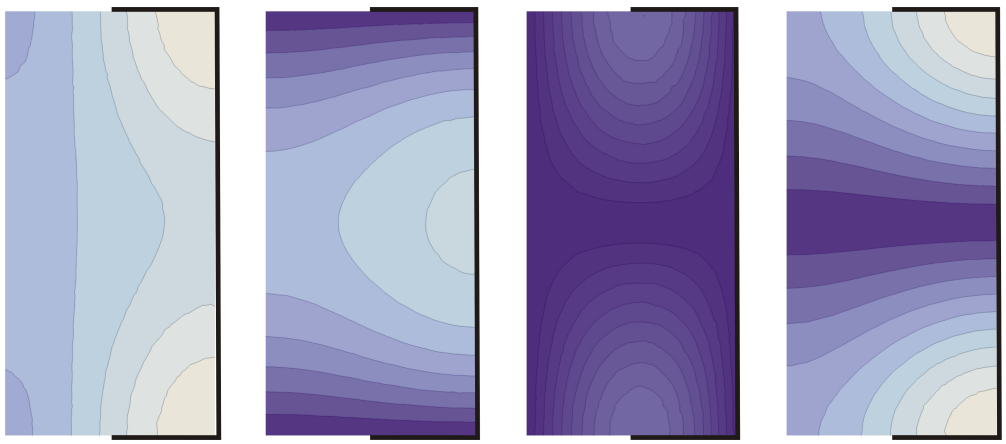

Figure 3.6: *Rectangular Waveguide Solutions using Ansoft HFSS. Slot cut 50% deep from right side. The magnetic field profile components are (a) magnetic field magnitude, (b) $\hat{x}$-component, H_x, (c) $\hat{y}$-component, H_y, (d)$\hat{z}$-component, H_z. Each contour represents a 10% change in amplitude.*

along with the evanescent roll off in $\pm\hat{z}$-directions. This is not apparent in current EPR literature, where the quasi-static field is assumed to create modes that are uniform over the cross-section of the sample.

Solution along the $\pm\hat{z}$-axis.

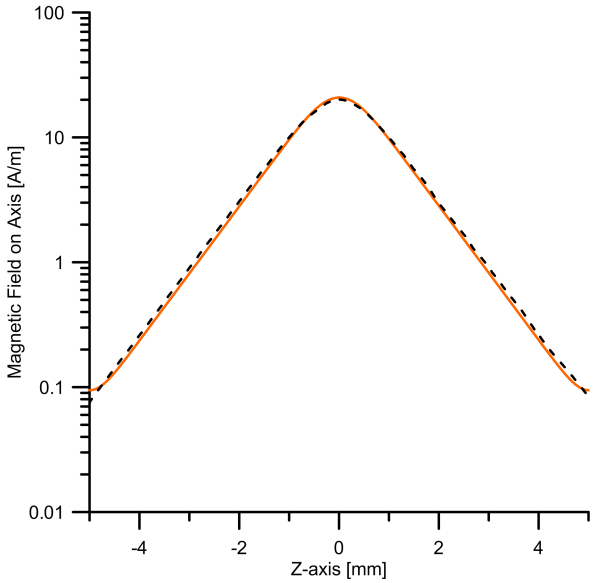

Figure 3.7: *Magnetic field profile for the rectangular waveguide $\hat{z}$-axis. Plotted is the Ansoft HFSS solutions (dashed) and the dyadic Green's function solution using magnetic surface current filament and convolution technique, M_s (orange). An RMSE of 0.306678 was calculated.*

Confidence in the magnetic field profile along the axis of the sample is crucial to the analysis of single and multiple slot configurations. Comparison of Ansoft and dyadic Green's function solutions down the $\pm\hat{z}$-axis result in a RMSE of 0.306678, using Eqn. 2.106. The results are plotted in Fig. 3.7 where the dyadic Green's function solution using magnetic surface current filament and convolution technique, Eqn. 3.8, is plotted alongside Ansoft HFSS solutions. The upward trend of the magnetic field at the edges of the solution on axis is an artifact of the convolution. The last 0.5 mm on each end are ignored in the RMSE calculation. Without the artifacts the solution should decay at an exponential rate and this rate is used as the criteria for the comparison.

Magnetic Field Amplitude

The data plotted in Figs. 3.5, and 3.6 are all normalized to the peak magnetic field magnitude in each solution. This normalization is used to gain confidence in the overall shape of the field profile, while the magnetic field amplitude is needed to gain confidence in the accuracy of the dyadic Green's functions.

Shown in Fig. 3.8 is the magnetic field magnitude on axis in the waveguide cross-section 1 mm from the slot source. This data represents the field profile plotted in the center of Fig. 3.6a. As the slot depth, ρ, is varied in depth the peak magnetic field magnitude increases lineally. Differences between Ansoft solutions and dyadic Green's functions are calculated yielding an RMSE of 0.0491084.

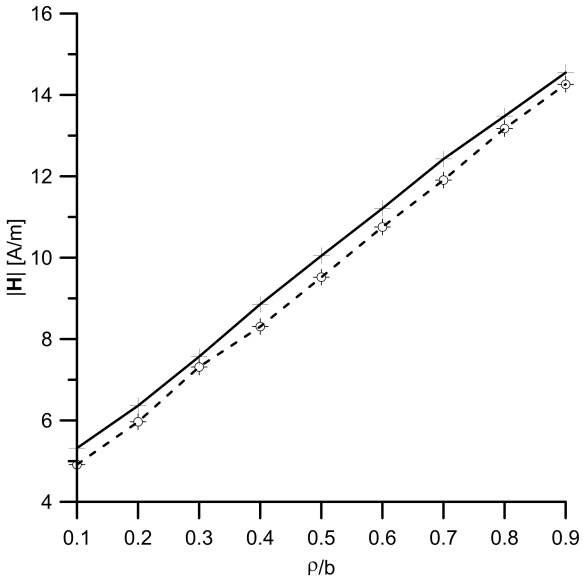

Figure 3.8: *Variations in the magnetic field on axis as the slot depth ρ is varied. Ansoft HFSS data (solid) is directly compared to dyadic Green's function solution (dashed). The RMSE of the solutions is 0.0491084.*

The variation in magnetic field magnitude relates directly to the slot depth. Simulations of the different slot depths show the peak electric field in the slot only varies by 15%. where the overall magnitude varies by 42%. The determining factor of the magnetic field magnitude is the rise and fall rate of the half-sinusoidal curve described as sections **A** and **C** in Fig. 2.13. The magnetic current profile for a slot depth of 0.1 a, 0.5 a, and 0.9 a is plotted in Fig. 3.9.

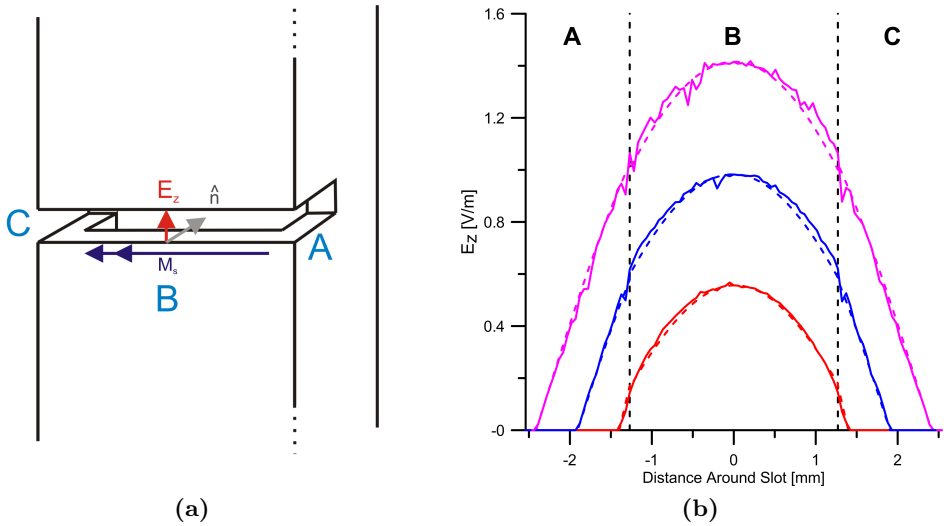

(a) (b)

Figure 3.9: *Variations in magnetic current profile around the slot shown for slot depths of 0.1 a, 0.5 a, and 0.9 a, red, blue, and purple, respectively. Ansoft simulations are shown in solid lines, where dashed lines are a sinusoidal approximation used for the source of the dyadic Green's function.*

The sinusoidal curves shown in Fig. 3.9 are plotted within the domain in the center of the slot, shown in Fig. 3.9a. The slot depth, ρ, is varied and the electric field in $\hat{z}$-direction follows the slot. The result is an overall increase of magnetic current amplitude along the slot. In the dyadic Green's function solution the dashed sinusoids are used as the electric field to calculate the magnetic current source.

Magnetic Field Phase

In EPR, the differential phase of the field modulation incident on the sample is as important as the amplitude. In the formulation of the Green's functions no assumptions are made of the nature of the propagation, unlike quasi-static approximations, where the phase variation within the domain is assumed to be zero.

The phase reference used is the slot itself within the domain. Comparison of Ansoft HFSS and dyadic Green's functions is shown in Fig. 3.10. The $\hat{x}$-component, the component of interest, shown in Fig. 3.10a, has very little variation within the domain. Slight variation, less than 0.1%, in the $\hat{x}$ and $\hat{y}$-component is present in the numerical results. Interesting results are shown for the $\hat{z}$-component of the phase, shown in

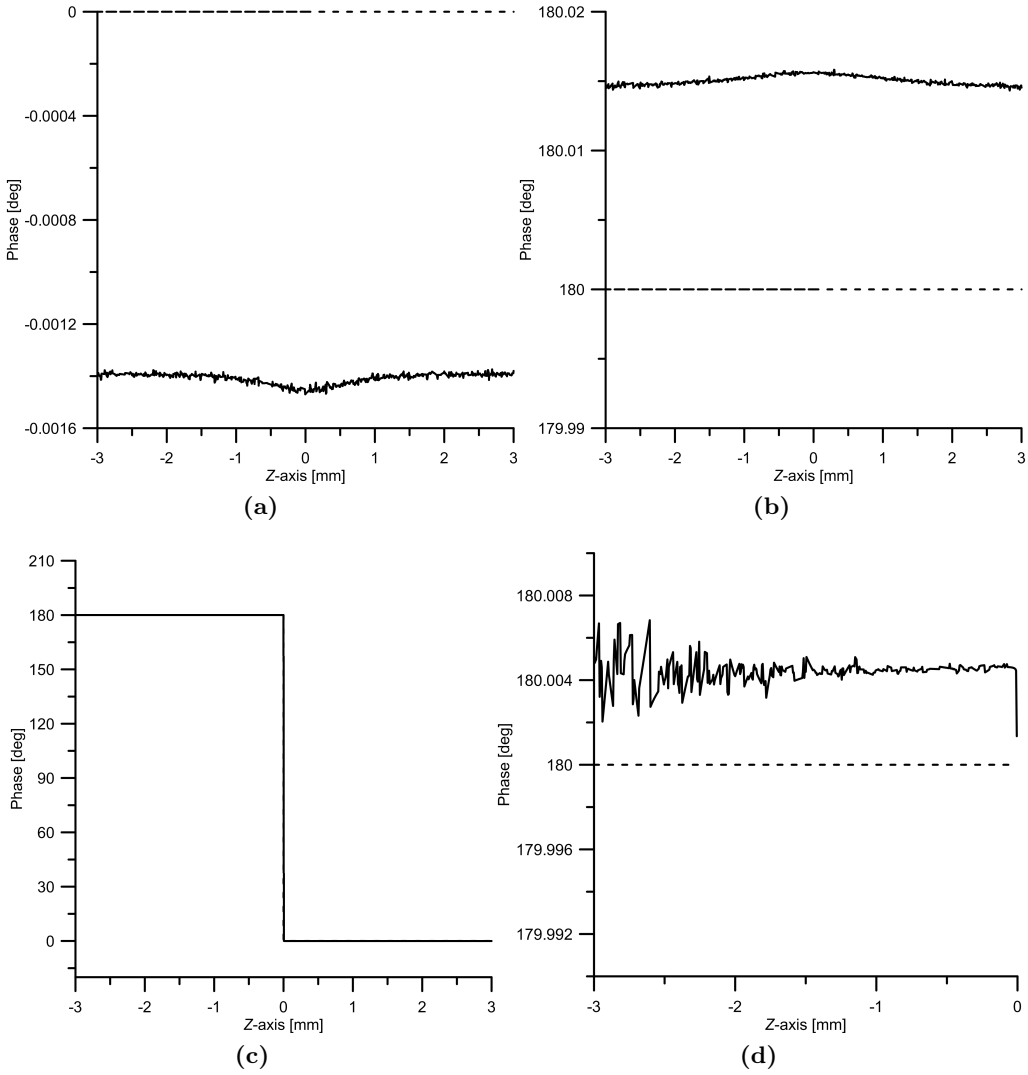

Figure 3.10: *Plot of the magnetic field phase component along the $\hat{z}$-axis. The (a) $\hat{x}$-component, (b) $\hat{y}$-component,and (c) and (d) $\hat{z}$-component using Ansoft data (solid) and numerical solutions (dashed) are compared for agreement. In both solutions the reference phase was at $x = 0$ and $y = 0.25a$.*

Table 3.1: *Phase between excitation coil and domain.*

Component	**Amplitude** [A/m]	**Phase** [deg]
x	11.3324	-0.016
y	1.70746	4.3585
z	1.05329	-180

Fig. 3.10c. Here the phase of the positive wave (+$\hat{z}$-direction) has a phase of 180 degrees, while the negative wave (-$\hat{z}$-direction) has no phase change. The phase change of the $\hat{z}$-component is in reference to the field position and propagation from the slot. No significant phase variation along the slot was found in either numerical or analytical results.

Another important phase is between the excitation coil outside the domain and the slot inside the domain. This phase relationship is characterized using Ansoft HFSS and reported in Table 3.1. The phase relationship between the coil and the domain remain consistent with the understanding of field propagation into the domain. The $\hat{x}$-component, the component of interest, has very little variation between the coil and the domain. This is the case because the eddy currents around the slot on the outside of the waveguide walls maintain the relationship between the coil fields and inside the domain. Since the coil should not have a $\hat{y}$-component, no $\hat{y}$-component variation should be expected. The variation that is shown is hypothesized from the "bending" of the current around the slot. Likewise, since the coil should not have a $\hat{z}$-component, no $\hat{z}$-component variation should be expected. In this case, the $\hat{z}$-component is 180 degrees out of phase and cancels the components in the slot. The amplitude of both the $\hat{y}$ and $\hat{z}$-component is small relative to the $\hat{x}$-component of the excitation field.

3.4 Single Slot Cylindrical Results

The cylindrical geometry used for the formulation of the solution is illustrated in Fig. 3.11. The lowest order mode that propagates in the cylindrical waveguide with a radius of 3.175 mm is the TE_{11} with a cut-off frequency of 55.338 GHz, which makes 100 kHz well below propagation cut-off. The propagation of all modes coupling into the waveguide are then evanescent.

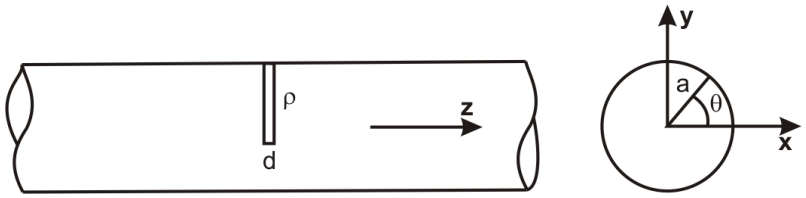

Figure 3.11: *Definition of the cylindrical geometry with a slot. The radius a is 3.175 mm and the center of the slot is located on the xy-plane with a depth, ρ, of 3.175 mm and a thickness, d, of 0.05 mm.*

Similar to the rectangular results, a sinusoidal electric field in the $\hat{z}$-direction is used to create the magnetic current around the slot. In the case for the cylindrical waveguide, more electric field is shown to exist in the slot. This is illustrated in Fig. 3.12.

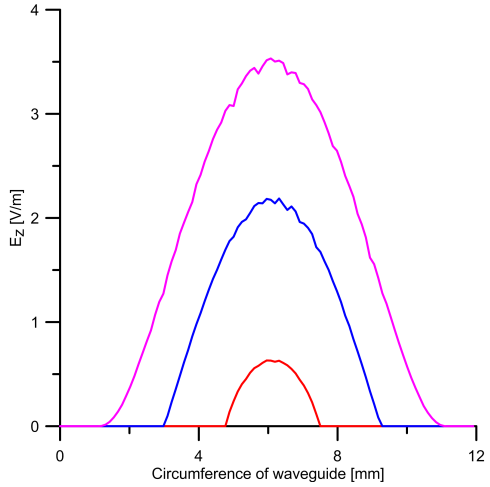

Figure 3.12: *Variations in a magnetic current profile around a cylindrical slot for depths of 0.1a (red), 0.5a (blue) and 0.9a (purple).*

A two-dimensional contour plot of the evanescent mode solutions using the dyadic Green's functions and the convolution techniques described in Section 3.2, are shown in Fig. 3.5. The contour plots are of the normalized magnetic field magnitude (H_{abs} shown in Fig. 3.13a) and the individual vector components: H_x, H_y, and H_z; Figures 3.13b, 3.13c, 3.13d, respectively. The slot source was a single slot cut into the right face of the waveguide in the $\hat{y}$-direction with a slot thickness, d, of 0.05 mm. For the initial results the slot depth was half the waveguide thickness, ρ is 3.175 mm. The slot cut is indicated in all figures as a black outline. The applied magnetic field is uniform and in the $\hat{x}$-direction. In the dyadic Green's functions ten TE modes were used and ten TM modes

were used for the best convergence.

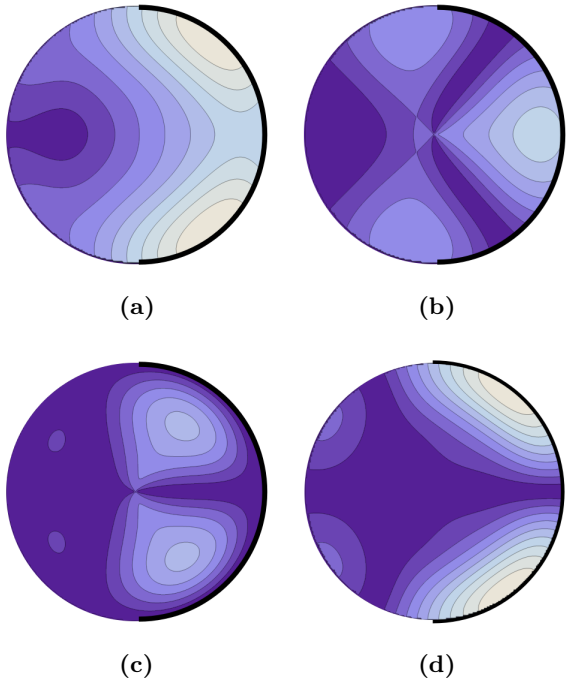

Figure 3.13: *Cylindrical Waveguide Solutions using dyadic Green's Functions. Slot cut 50% deep from right side. Each contour represents a 10% change in amplitude. The magnetic field profile components are (a) magnetic field magnitude, (b) $\hat{x}$-component, H_x, (c) $\hat{y}$-component, H_y, (d)$\hat{z}$-component, H_z.*

The results are visually compared to Ansoft HFSS data, shown in Fig. 3.14. Good agreement between analytical and numerical results are shown. The results from the dyadic Green's functions show a slightly larger gradient of magnetic field in the $\hat{y}$-direction.

Solution along the $\pm\hat{z}$-axis.

Confidence in the magnetic field profile along the axis of the sample is crucial to the analysis of single and multiple slot. Comparison of Ansoft and dyadic Green's function solutions down the $\pm\hat{z}$-axis result in a RMSE of 0.220807, using Eqn. 2.106. The results are plotted in Fig. 3.15 where the dyadic Green's function solution using magnetic surface current filament and convolution technique, Eqn. 3.8, is plotted along side the Ansoft HFSS solutions. The upward trend of the magnetic field at the edges of the solution on

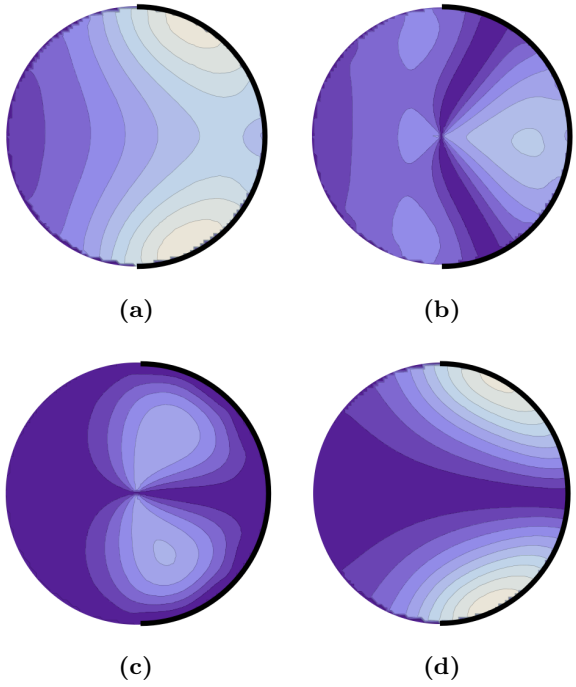

Figure 3.14: *Cylindrical Waveguide Solutions using Ansoft HFSS. Slot cut 50% deep from right side. Each contour represents a 10% change in amplitude. The magnetic field profile components are (a) magnetic field magnitude, (b) $\hat{x}$-component, H_x, (c) $\hat{y}$-component, H_y, (d)$\hat{z}$-component, H_z.*

axis is a byproduct of the convolution. The ends are ignored in the RMSE calculation.

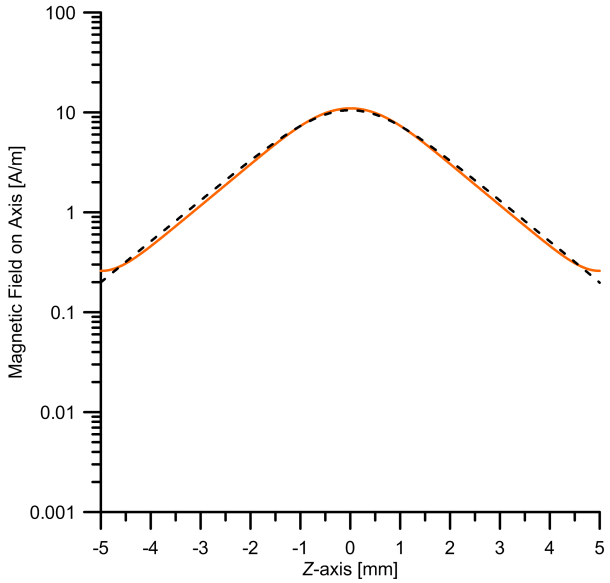

Figure 3.15: *Magnetic field profile for the cylindrical waveguide $\hat{z}$-axis. Plotted is the Ansoft HFSS solutions (dashed) and the dyadic Green's function solution using magnetic surface current filament and convolution technique, M_s (orange). An RMSE of 0.220807 was calculated.*

Chapter 4: Discussion

4.1 Multiple Slot Formulation

Solutions between Ansoft HFSS simulations and dyadic Green's function solutions show good agreement for both cylindrical and rectangular results. Confidence in the magnetic field cross-section and amplitude down axis is presented in the previous sections. From these single slot solutions a multiple slot formulation can be devised. Two methods are used in the formulation of the interactions between multiple slots, simple summation of the slot fields and a first-order moment method to include mutual coupling.

The multiple slot calculations were performed with the rectangular waveguide geometry from Section 3.3 but are also valid for cylindrical results.

4.1.1 Summation of Multiple Slot Fields

In the formulation of multiple slots, the dyadic Green's functions were modified to displace the feed point in the $\hat{z}$-direction. This is done by changing the z' variable in the dyadic Green's function in Eqn. 2.86 or Eqn. 2.100. Two solutions are then created at a $\pm z'$ distance resulting in slot spacings of 5.08 mm, 2.54 mm, and 0.508 mm. The second slot depth, ρ_2, is then varied as $0.3a$, $0.5a$, and $0.7a$. These depths were chosen because they are practical depths in construction of field modulation slots. In this calculation the number of modes used were ten TE modes and nine TM modes. Using more modes did not significantly change the RMSE. The solutions were simply summed together to create the initial zero-order results.

Using Ansoft HFSS the slots were varied in both position and in depth, the same as the dyadic Green's function. With HFSS, both slots were excited by the Helmholtz coils from outside the domain as expected in a real experiment. The results are then compared visually and by calculating the RMSE value using Eqn. 2.106.

If the two slots are independent from each other a simple summation of the slot fields should completely describe the multiple slot system. In this case, as evidenced in Fig. 4.1, the Ansoft HFSS calculations (solid) do not validate with the dyadic Green's solutions (dashed).

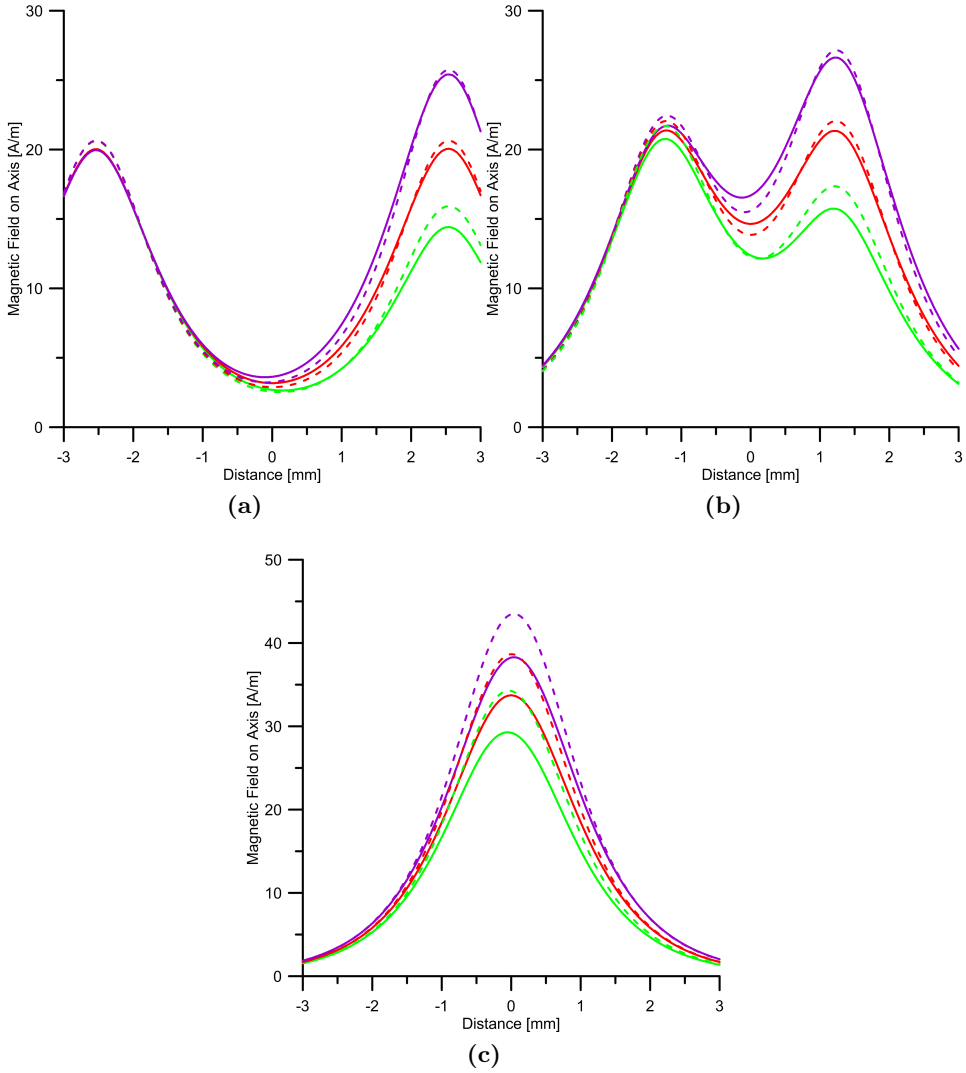

Figure 4.1: *Multiple slot configurations using a simple summation of the slot fields. The first slot is at 0.5a while the second slot is varied: 0.3a (green), 0.5a (red), and 0.7a (purple). The solutions are displayed using a linear plot to emphasize the variation between Ansoft(solid) and dyadic Green's functions (dashed) solutions. Slot distances are (a) 5.08 mm, (b) 2.54 mm, and (c) 0.508 mm apart.*

Table 4.1: *RMSE calculations for a simple summation of multiple slot fields.*

Distance [mm]	ρ_1/**a**	ρ_2/**a**	**RMSE**
5.08	0.5	0.3	0.626165
5.08	0.5	0.5	0.404064
5.08	0.5	0.7	0.543898
2.54	0.5	0.3	0.683480
2.54	0.5	0.5	0.427618
2.54	0.5	0.7	0.535444
0.508	0.5	0.3	1.181602
0.508	0.5	0.5	1.372851
0.508	0.5	0.7	1.331543

Figure 4.1 illustrates a number of experimental comparisons between Ansoft HFSS and dyadic Green's function solutions. Table 4.1 contains the RMSE for each of the comparisons in Fig. 4.1. The solutions are displayed using a linear plot to emphasize the variation between the two calculations.

When the solutions are "far enough" apart[1], they have little interaction with each other. This is shown in Fig. 4.1a, where the slots are 5.08 mm apart from each other and the RMSE for the slots having the same depth are comparable to the single slot RMSE of 0.306678. The majority of the error arises from the region between the slots. It appears that the effective roll-off between the slots is shifted. Increasing the number of modes had no effect in reducing the error between the slots.

As the slots are moved closer together to 2.54 mm apart, shown in Fig. 4.1b, the interactions of the slots start to change. In general, the RMSE raises only slightly but the region containing error is significantly different. More error arises from the region at the slots, which has the largest effect on the RMSE and the validity of the solution.

When the slots become too close, the dual peaks shown in Figs. 4.1a and 4.1b have merged into one. At this distance, 0.508 mm in Fig. 4.1c, the Ansoft HFSS solutions are significantly smaller than the simple summation of the slot fields from the dyadic Green's functions. The RMSE error of 1.9 is approximately 4 times larger than the other two cases.

The summation of the slots only takes into account the magnetic field from the

[1]The term "far enough" is defined by observing the evanescent roll-off of each peak individually. In this work, if the evanescent field is more than a factor of ten down in amplitude by the time it reaches the other slot position it is defined as "far enough".

excitation of the slots. Since the physical slots were removed in the formulation of the dyadic Green's function, the *mutual coupling* that may occur between the slots is neglected. Mutual coupling is defined as the interactions between the two slots that are not accounted for by the excitation of the individual slots.

Since Ansoft HFSS takes into account the whole geometry, an experiment was conducted to determine the profile of the mutual coupling. In the experiment two slots were cut into a PEC waveguide wall at a depth of $0.5a$. The first slot was excited with a E_z profile similar to the $0.5a$ curve of Fig. 3.9b.

The first experiment removed the second slot and varied the first slot relative to the center of the waveguide. At each sweep value the magnetic field profile down the z-axis was recorded. The second experiment involved two slots, one driven and the other cut but not driven. Both slots were varied relative to the center creating a range of distances between the slots of 0.254 mm to 5.08 mm. At each step value the magnetic field profile down the z-axis was recorded.

In experiment one, as the slot moved along the waveguide only the peak position of the magnetic field down the z-axis changed relative to the position of the slot. No change in the amplitude was recorded. In the second experiment, as the slots became closer together the value of the magnetic field peak decreased. By taking the difference of the control experiment and the two slot experiment a residual magnetic field caused by the mutual coupling between the first and second slot could be found. These results are illustrated in Fig. 4.2.

Figure 4.2a shows the peak value of the residual magnetic field as the slot distance was varied. The peak value being negative is significant for two reasons. The first is that a negative value would subtract from the overall magnetic field profile, as expected from studying Fig. 4.1c. The second significance is in the understanding of how the mutual coupling arises in the coupled system. A field excited by slot one imposed on slot two would create an E_z in the opposite polarity of the excited slot.

In Fig. 4.2b, the residual magnetic field along the z-axis is plotted for the three distances exampled in this work: 5.08 mm, 2.54 mm and 0.508 mm. As expected when the second slot is moved, the position of the residual magnetic field peak moves. When the

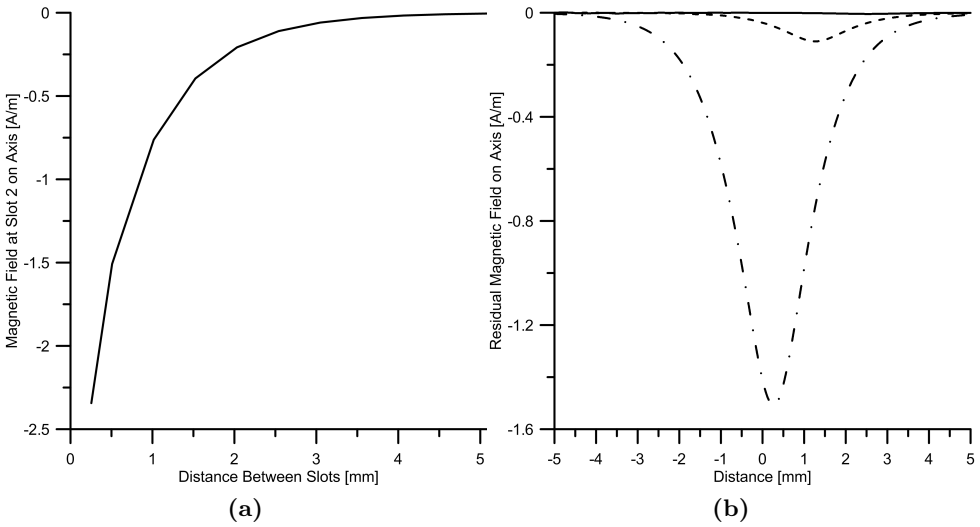

Figure 4.2: *(a) Mutual coupling interaction is plotted versus the distance between two slots. (b) The shape of the field presented down axis due to the mutual coupling between the two slots is the same shape as if the a single slot was excited. Slot distances are 5.08 mm (solid), 2.54 mm (dashed) and 0.508 mm (dash-dot).*

slots are 5.08 mm apart, very little mutual coupling exists.

The mutual coupling between multiple slots must be accounted for in order to reduce the error between the Ansoft HFSS and dyadic Green's function solutions. In this work, a first-order moment method is implemented in order to characterize and fully account for the phenomenon of mutual coupling.

4.1.2 Moment Method

The *moment method* is a way to describe the total response at a given point caused by two or more stimuli as the sum of the individual responses and the sum of the responses on each stimuli caused by the other stimuli. This can be visualized by Fig. 4.3, where the wave propagating from the first slot, shown in black, at the feed point of the second slot is used to calculate a residual magnetic field, shown in red dashed. In this work the magnetic field is 180 degrees out of phase from the primary magnetic field of the second slot, reducing the overall effect of the slot solution. At the same time the reciprocal problem is occurring.

The moment method being used is said to be of "first-order". In this work,

first-order is used to describe the summation of the initial simple summation (zero-order) and the mutual coupling interaction between the slots (first-order). For example, second-order would include the mutual coupling of the fields created by the first-order mutual coupling.

Standard S-parameter notation will be used in describing the mutual coupling where the second index is reserved for the excitation and the first for the position. Thus $\overline{H}_{12}$ describes the magnetic field at slot one, excited by slot two.

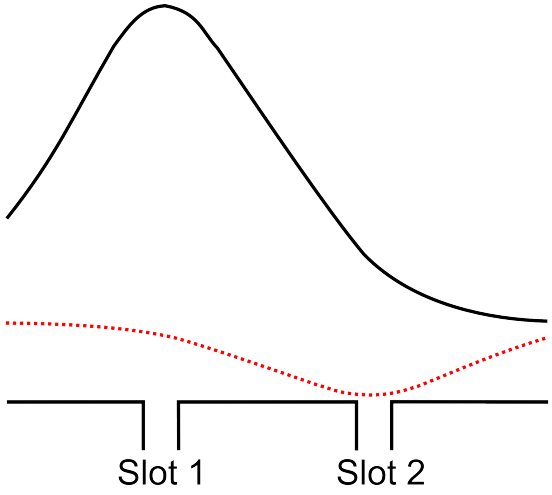

Figure 4.3: *Visualization of the moment method. Slot one's electric field induces a voltage drop across slot two which creates a residual magnetic field that reduces the primary magnetic field induced by the second slot. The moment method phenomenon is reciprocal.*

The moment method has been used in the literature as an evaluation technique to calculate the mutual coupling between micro-strip antenna arrays [48, 49, 50, 51]. Using reciprocity, a voltage is applied on one slot and a current is measured across the other slot. This thought process mimics the experiment performed to characterize the mutual coupling in Fig. 4.2. This work follows the methods described by Pan and Pozar, [48] and [49] respectively.

In Refs. [48] and [49] a voltage reflection current is defined on the surface from an incident field driven by the ith slot onto the jth slot. The reflection magnetic current is defined as

$$\overline{R}_{ji} = i\omega\mu \int \overline{\overline{G}}_m^j \overline{M}_f^{ji} d\Omega, \tag{4.1}$$

where M_f^{ji} is the jth filament magnetic current centered at the position of the jth slot calculated from the ith source, $\overline{\overline{G}}_m^j$ is the expected modal solution of the magnetic field from the dyadic Green's functions located at the jth slot and Ω is the 2.5-dimensional line around the waveguide walls centered at the jth slot. From here the magnetic field driven from the ith slot at the jth slot is calculated by

$$\overline{H}_{ji} = \int \overline{\overline{G}}_m^j \cdot \overline{R}_{ji} d\Omega \text{ for } i \neq j. \tag{4.2}$$

Since this work uses only two slots, the magnetic current can be solved for directly using the dyadic Green's functions knowing the magnetic field from the first slot, the magnetic current on the second slot can be calculated. If more slots were being considered a matrix would be created taking into effect all the slot interactions. The total solution is then the summation of the slots plus the first-order solution, such that

$$\overline{H}_{tot} = \overline{H}_{11} + \overline{H}_{22} + (\overline{H}_{21} + \overline{H}_{12}). \tag{4.3}$$

It should be noted that $\overline{H}_{21}$ and $\overline{H}_{12}$ result in magnetic fields that oppose the superimposed fields, yielding a lower total magnetic field as expected from Fig. 4.2.

Using the moment method solutions were calculated for slot distances of 5.08 mm, 2.54 mm and 0.508 mm. In these calculation the first slot, ρ_1, constant at $0.5a$ while the second slot, ρ_2, is varied between $0.3a$, $0.5a$, and $0.7a$. The results of these calculations can be found in Table 4.2. Additionally, in Fig. 4.4 a comparison of Ansoft HFSS (black), simple summation (blue), and first-order moment method (green) solutions down the axis of the rectangular waveguide is plotted for the 0.508 mm case. The solutions are displayed using a linear plot to emphasize the variation between the solutions.

Table 4.2 shows some mixed results between the RMSE of the simple summation solutions, RMSE_s, and the first-order method moment, RMSE_m. For variations of slot distance and slot depths of $0.3a$ and $0.5a$, the moment method decreased the RMSE as expected. The issue arises in the results where the second slot depth was $0.7a$, where in all cases the RMSE increased.

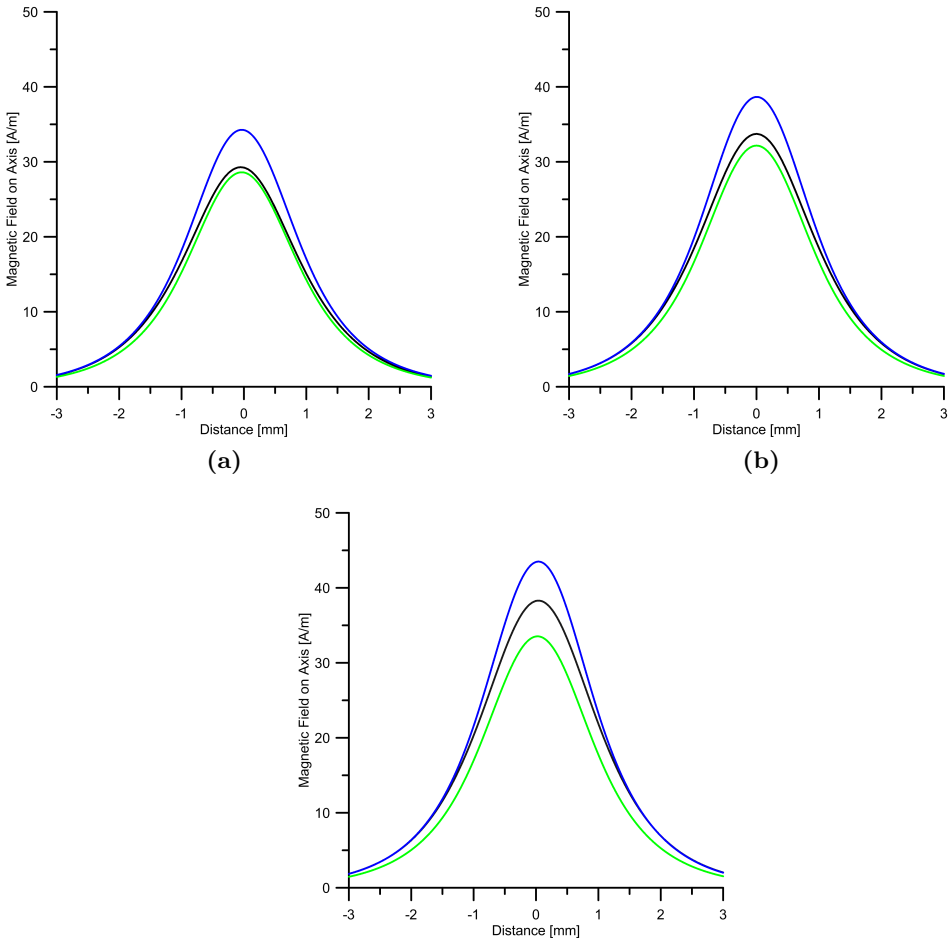

Figure 4.4: *Multiple slot configurations using first-order moment method. The first slot is at 0.5a while the second slot is varied: (a) 0.3a, (b) 0.5a, and (c) 0.7a. The solutions are displayed using a linear plot to emphasize the variation between Ansoft (black), simple summation (blue), and first-order moment method (green) solutions. Slot distance is 0.508 mm apart.*

The issue of the increased RMSE in the case where the second slot depth is $0.7a$ is not due to the accuracy of the moment method, instead due to changes in the system from outside of the domain. To test this hypothesis the two slots were moved to 0.254 mm apart which would increase mutual coupling between the slots. If the anomaly is from the moment method, then increasing the mutual coupling should increase the error. This is shown not to be the case by observing Table 4.2. Here the exact phenomenon of an increasing RMSE occurs at the second slot depth of $0.7a$ at a distance of 0.254 mm while

Table 4.2: *RMSE calculations for first-order moment method multiple slot formulation. RMSE values for simple summation formulation, $RMSE_s$, and moment method, $RMSE_m$, are directly compared.*

Distance [mm]	ρ_1/**a**	ρ_2/**a**	**RMSE**$_s$	**RMSE**$_m$
5.08	0.5	0.3	0.626165	0.508758
5.08	0.5	0.5	0.501948	0.404064
5.08	0.5	0.7	0.543898	0.781346
2.54	0.5	0.3	0.683480	0.489288
2.54	0.5	0.5	0.639576	0.427618
2.54	0.5	0.7	0.535444	1.026530
0.508	0.5	0.3	1.181602	0.415276
0.508	0.5	0.5	1.372851	1.153870
0.508	0.5	0.7	1.331543	2.894110
0.254	0.5	0.3	2.29347	0.478667
0.254	0.5	0.5	2.30797	1.087350
0.254	0.5	0.7	2.24897	3.034104

the other two slot depths are improved.

Shown in Fig. 4.5, the magnitude of the eddy currents outside the waveguide for a distance of 0.254 mm are plotted. In Figs. 4.5a and 4.5b a strong mutual coupling between the two slots and a relatively unperturbed surface current located on the opposite side of the slot is shown. However, in the case of $0.7a$, shown in Fig. 4.5c, a different phenomenon not included within the domain is seen in the interaction of the currents opposite of the slot cuts. From this interaction the mutual coupling between slot two and slot one decreases resulting in an inaccurate moment method interaction.

If each slot was driven from independent sources addition of the slot magnetic fields would be sufficient to obtain the field profile down axis. Instead additional terms must be added to the solution to account for slot to slot interactions. Since all slots are driven with a single incident wave and the electric field in the slot is dependent on eddy currents formed by scattered waves outside the domain, the results are non-trivial under some conditions. With this complexity arising from slot-to-slot interaction outside the domain, it would prove difficult to fully express in an analytical solution.

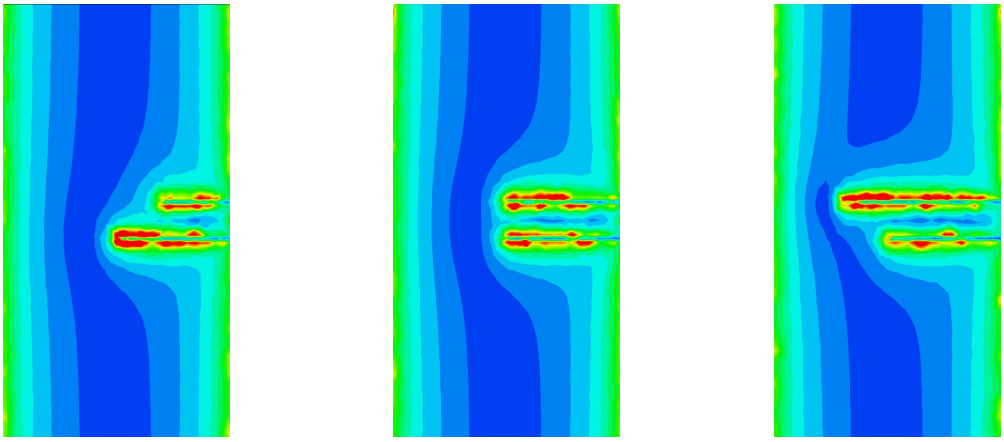

(a) **(b)** **(c)**

Figure 4.5: *Numerical solution to magnitude of eddy currents outside the waveguide domain using Ansoft HFSS. Slots are located 0.254 mm apart. Slot one is cut 0.5a deep and slot two is varied between (a) 0.3a, (b) 0.5a, and (c) 0.7a.*

Chapter 5: Conclusion

Dyadic Green's functions have shown to be useful in the understanding of evanescent field coupling to slots cut into waveguide walls. By using a Gaussian function instead of a Unit Step function, as assumed by Born's first approximation, near field secondary wave effects are included to produce an accurate profile of the magnetic current inside a waveguide for slots much smaller than a wavelength can be determined. The physical slots are removed using the equivalence principle to provide a valid domain for the dyadic Green's functions. If the physical slots did not interact with each other, a simple summation of slot contributions would be adequate to describe the multiple slot solution.

Interactions arising from multiple slots can be understood using a combination of simple summation and mutual coupling techniques to account for the slots that are removed during the formulation of the magnetic current profile. However, the analytical methods are limited due to eddy current changes outside the domain that cannot be accounted for directly in the dyadic Green's function solution. For final evaluation, Ansoft HFSS solutions have proven to be accurate by simulating the full geometry.

Electromagnetic modes forming from the 100 kHz time-varying source are shown to have a complex cross-section which has not been previously documented in EPR literature. With a cross-section that is irregular, the placement of the sample and sample geometry will have an effect on the magnetic field strength applied to the sample.

With the design of a uniform RF and field modulation microwave cavity, field scan experiments at W-band (94 GHz) are feasible. This advance in EPR spectroscopy will allow for pure absorption signals to be collected or better quantitative results for typical continuous-wave experiments. This enables the next generation of W-band spectroscopy. The proposed uniform RF and field modulation structure can be built using precision EDM technology. Since the structure is fabricated from a single piece of silver, the acoustic resonance caused by the Lorentz forces will be much lower than the 100 kHz field modulation. In previous work, the field modulation phase and amplitude were always uncertain and now can be analyzed in detail. The combination of numerical and analytical tools coupled with ultra precise fabrication technology has created an opportunity for

optimized cavity design that has only become realized in the last ten years.

5.1 Recommendations and Future Work

This work focused on slots cut in a waveguide that was infinitely long. Further research can be conducted using the tools outlined here with modifications to the dyadic Green's function to include the cavity end sections. This would include the change in waveguide geometry outside the region-of-interest and the effect the cavity wall at the $\pm z$ ends. Works by Mett et al. in Ref. [52] and Štafl et al. in Ref. [45] touch on this subject. Additional work can be performed with varying the slot thickness, in this work the slot thickness is always 0.0508 mm.

More work could be done on the mutual coupling formulation including expanding to more than two slots. Following Pan and Pozar, Refs. [48] and [49] respectively, in the characterization of multiple antenna arrays a magnetic current matrix can be constructed and solved for more than two slots. Interactions of the slots outside the domain can be characterized using eddy current analytical formulations like the Boundary Element Method (BEM). The eddy current BEM, proposed by Ishibashi [53], would prove useful in the understanding of the surface currents on a finite geometry. Ishibashi's work is more rigorous than the works cited in this thesis [44, 45]. Advantages of BEM can be found in Ref. [54].

Work can be done on optimizing the magnetic field uniformity in the cross-section of the rectangular and cylindrical waveguide. A suggestion would be to look into cutting slots at different angles from the applied magnetic field. This work only used slots cut in the -y-direction. Slots that are cut in the $\pm x$-direction may prove beneficial in exciting modes in the waveguide that would add constructively with the field profiles expressed here.

Finally, variations in frequency or harmonic content (such as with triangle or pulsed sweeps) of the applied time-varying magnetic field can be looked at in more detail. Phase variations, eddy current formation outside the domain, and modes within the waveguide will all be affected by the frequency of modulation.

BIBLIOGRAPHY

[1] C. P. Poole, *Electron Spin Resonance: A Comprehensive Treatise on Experimental Techniques.* John Wiley & Sons, 1967.

[2] G. E. Pake, *Paramagnetic Resonance.* W.A. Benjamin, Inc., 1962.

[3] T. K. Ishii, *Handbook of Microwave Technology, Vol. 2 Applications.* Academic, 1995, see especially Fig. 27, p. 398.

[4] R. R. Mett, W. Froncisz, and J. S. Hyde, "Axially uniform resonant cavity modes for potential use in electron paramagnetic resonance spectroscopy," *Rev. Sci. Instrum.*, vol. 72, p. 4003, 2001.

[5] J. R. Anderson, R. R. Mett, W. Froncisz, and J. S. Hyde, "Cavities with axially uniform fields for use in electron paramagnetic resonance. II. Free space generalization," *Rev. Sci. Instrum.*, vol. 73, p. 3027, 2002.

[6] J. S. Hyde, J. R. Anderson, and R. R. Mett, "Cavities with axially uniform fields for use in electron paramagnetic resonance. III. Re-entrant geometries," *Rev. Sci. Instrum.*, vol. 73, p. 4003, 2002.

[7] J. S. Hyde, "Endor of free radicals in solution," *J. Chem. Phys.*, vol. 43;5, 1965.

[8] L. Blyumenfel'd, V. Voyevodskiy, and A. Semenov, "Application of electron paramagnetic resonance in chemestry," *Foreign Technology Division; Air Forces Systems Command*, vol. FTD-MT-64-306, 1966.

[9] M. Weger, "Passage effects in paramagnetic resonance experiments," *Bell System Tech. J.*, vol. 39, p. 1013, 1960.

[10] J. Hyde, M. Pansenkiewicz-Gierula, A. Jesmanowicz, and W. E. Antholine, "Pseudo field-modulation in EPR spectroscopy," *App. Mag. Res.*, vol. 1, p. 483, 1990.

[11] J. P. Joshi, J. R. Ballard, G. A. Rinard, R. W. Quine, S. S. Eaton, and G. R. Eaton, "Rapid-scan epr with triangular scans and Fourier deconvolution to recover the slow-scan spectrum," *J. Magn. Reson.*, vol. 175;1, pp. 44 – 51, 2005.

[12] P. A. Berger and H. Günthart, "The distortion of electron spin resonance signal shapes by finite modulation amplitudes," *Math. Phys.*, vol. 13, pp. 310–323, 1962.

[13] J. W. Sidabras, R. R. M. W. Froncisz, T. G. Camenisch, J. R. Anderson, and J. S. Hyde, "Multipurpose EPR loop-gap resonator and cylindrical TE_{011} cavity for aqueous samples at 94 GHz," *Rev. Sci. Instrum.*, vol. 78, 2007.

[14] F. Bloch, "Nuclear induction," *Physics Review*, vol. 70, pp. 460–473, 1946.

[15] R. R. Mett, J. W. Sidabras, and J. S. Hyde, "Coupling of waveguide and resonator by inductive and capacitive irises for EPR spectroscopy," *Applied Magn. Res.*, vol. 35;2, pp. 285–318, 2009.

[16] V. Krymov and G. J. Gerfen, *J. of Mag. Reson.*, vol. 162, pp. 466–478, 2003.

[17] T. C. Christidis and F. W. Heineken, "A cylindrical TM_{110} endor cavity," *J. Phys. E: Sci. Instrum.*, vol. 18, 1985.

[18] T. H. Wilmshurst, *Signal Recovery from Noise in Electronic Instrumentation*, 2nd ed. IOP Publishing, 1990.

[19] J. S. Hyde and L. Dalton, "Very slowly tumbling spin labels: Adiabatic rapid passage," *Chem. Pys. Letters*, vol. 16;3, p. 568, 1972.

[20] J. S. Hyde, "U.s. patent no. 3,250,985," pp. 1806–1818, 1966.

[21] R. R. Mett and J. S. Hyde, "Microwave leakage from field-modulation slots in te_{011} electron paramagnetic resonance cavities," *Rev. Sci. Instrum.*, vol. 76, p. 014702, 2005.

[22] . Burghaus, M. Rohrer, and T. G "A novel high-field/high-frequency epr and endor spectrometer operating at 3 mm wavelength."

[23] J. A. Stratton, *Electromagnetic Theory.* McGraw-Hill, 1941.

[24] R. F. Harrington, *Time-Harmonic Electromagnetic Fields.* McGraw-Hill, 1961.

[25] C. Tai, *Dyadic Green's Functions in Electromagnetic Theory*, 2nd ed. IEEE Press, 1994.

[26] J. D. Jackson, *Classical Electrodynamics*, 3rd ed. John Wiley & Sons, 1999.

[27] R. E. Collin, *Field Theory of Guided Waves.* McGraw-Hill, 1960.

[28] P. M. Morse and H. Feshback, *Methods of Theoretical Physics: Part I.* McGraw-Hill, 1953.

[29] C. Tai, *Dyadic Green's Functions in Electromagnetic Theory*, 1st ed. International Textbook, 1971.

[30] P. M. Morse and H. Feshback, *Methods of Theoretical Physics: Part II.* McGraw-Hill, 1953.

[31] J. B. Conway, *Functions of One Complex Variable.* Springer Science+Business Media, 1978.

[32] L. W. Li, P. S. Kooi, M. S. Leong, T. S. Yeo, and S. L. Ho, "On the eigenfunction expansion of electromagnetic dyadic greens functions in rectangular cavities and waveguides," *IEEE Transactions on Microwave Theory and Tech.*, vol. 43;3, pp. 700–702, 1995.

[33] M. Born and W. Wolf, *Principles of Optics: Electromagnetic Theory of Propagation, Interference and Diffraction of Light*, 3rd ed. Pergamon Press, 1965.

[34] C. A. Balanis, *Advanced Engineering Electromagnetics.* John Wiley & Sons, 1989.

[35] C. M. Butler, Y. Rahmat-Samii, and R. Mittra, "Electromagnetic penetration through apertures in conducting surfaces," *IEEE Trans. on ElectroMag. Compat.*, vol. EMC 20;1, pp. 82–93, 1978.

[36] M. W. Kowarz, "Homogeneous and evanescent contributions in scalar near-field diffraction," *Applied Optics*, vol. 34;7, pp. 3055–3063, 1995.

[37] A. Hrennikoff, "Solution of problems of elasticity by the frame-work method," *ASME J. Appl. Mech.*, vol. 8, p. A6190A715, 1941.

[38] R. L. Courant, "Variational methods for the solution of problems of equilibrium and vibration," *Bulletin of the American Mathematical Society*, vol. 49, pp. 1–23, 1943.

[39] G. Pelosi, "The finite-element method, Part I: R. L. Courant [historical corner]," *IEEE Antennas and Propagation*, vol. 49;2, pp. 180–182, 2007.

[40] R. Ferrari, "The finite-element method, Part 2: P. P. Silvester, an innovator in electromagnetic numerical modeling," *IEEE Antennas and Propagation*, vol. 49;3, pp. 216–234, 2007.

[41] J. Tinsley, "Historical comments on finite-elements," *History of Scientific Computing, ACM*, pp. 152–166, 1990.

[42] J. Jin, *The Finite Element Method in Electromagnetics*, 2nd ed. John Wiley & Sons, 2002.

[43] W. R. Smythe, *Static and Dynamic Electricity*, 3rd ed. McGraw-Hill, 1968.

[44] R. Albanese and G. Rubinacci, "Formulation of the eddy-current problem," *IEE Proceedings*, vol. 137;A;1, 1990.

[45] J. Lammeraner and M. Štafl, *Eddy Currents*. CRC Press, 1964.

[46] A. Krawczyk and J. A. Tegopoulos, *Numerical Modeling of Eddy Currents*. Oxford Science Publications, 1993.

[47] M. N. O. Sadiku, *Numerical Techniques in Electromagnetics*, 2nd ed. CRC Press, 2001.

[48] S. Pan, "Computation of mutual coupling between slot-coupled microstrip patches in a finite array," *IEEE Trans. on Ant. & Prop.*, vol. 40;9, p. 1047, 1992.

[49] D. M. Pozar, "A reciprocity method of analysis. for printed slot and slot-coupled microstrip antennas," *IEEE Trans. on Ant. & Prop.*, vol. AP-32, No. 12, p. 1439, 1986.

[50] P. B. Katehi, "Mutual coupling between microstrip dipoles in multielement arrays," *IEEE Transactions on Antennas and Propagation*, vol. 37;3, p. 275, 1989.

[51] D. M. Pozar, "Input impedance and mutual coupling of rectangular microstrip antennas," *IEEE Transactions on Antennas and Propagation*, vol. AP-30;6, p. 1191, 1982.

[52] R. R. Mett, J. R. Anderson, J. W. Sidabras, and J. S. Hyde, "Electron paramagnetic resonance field-modulation eddy-current analysis of silver-plated graphite resonators," *Rev. Sci. Instrum.*, vol. 76, p. 094702, 2005.

[53] K. Ishibashi, "Eddy current analysis by BEM formulated by loop electric and surface magnetic currents utilizing edge boundary condition," *IEEE Trans. on Magnetics*, vol. 35;1, 1999.

[54] J. P. Webb, "Edge elements and what they can do for you," *IEEE Trans. on Magnetics*, vol. 29;2, 1993.

APPENDIX - Dyadic Mathematical Properties

The dyadic can be described as a tensor:

$$\overline{\overline{\mathscr{G}}} = \sum_i \sum_j \alpha_{ij} \hat{\mathbf{e}}_i \hat{\mathbf{e}}_j, \tag{A-1}$$

where i and j are in the set $\{1, 2, 3\}$. The normal vectors $\hat{\mathbf{e}}_i$ and $\hat{\mathbf{e}}_j$ can represent any orthonormal coordinate system. It important to note that

$$\hat{\mathbf{e}}_i \hat{\mathbf{e}}_j \neq \hat{\mathbf{e}}_j \hat{\mathbf{e}}_i. \tag{A-2}$$

A dyadic identity function, denoted by $\overline{\overline{I}}$, can be described as

$$\overline{\overline{I}} = \delta_{ij} \overline{\overline{\mathscr{G}}} = \sum_i \hat{\mathbf{e}}_i \hat{\mathbf{e}}_i = \hat{\mathbf{x}}\hat{\mathbf{x}} + \hat{\mathbf{y}}\hat{\mathbf{y}} + \hat{\mathbf{z}}\hat{\mathbf{z}}, \tag{A-3}$$

where δ_{ij} is known as the Kronecker delta function. If a dyadic is symmetrical, denoted by the subscript s, it implies that

$$\left[\overline{\overline{\mathscr{G}}}_s\right]^T = \overline{\overline{\mathscr{G}}}_s. \tag{A-4}$$

If a dyadic is asymmetrical, denoted by the subscript a, it implies that

$$\left[\overline{\overline{\mathscr{G}}}_a\right]^T = -\overline{\overline{\mathscr{G}}}_a. \tag{A-5}$$

Two important operations are the *scalar product* and the *vector product* between a vector and a dyadic. Since in general a dyadic is not symmetric, a vector acting on a dyad is known as an anterior operations and if a dyad is acting on a vector it is known as a

posterior operation. An anterior scalar product is defined as

$$\overline{\beta}(x,y,z)\cdot\overline{\overline{\mathscr{G}}}(x,y,z)=(\beta_x\hat{\mathbf{x}}+\beta_y\hat{\mathbf{y}}+\beta_z\hat{\mathbf{z}})\cdot\begin{bmatrix}\alpha_x^1\hat{\mathbf{x}}\hat{\mathbf{x}} & \alpha_x^2\hat{\mathbf{x}}\hat{\mathbf{y}} & \alpha_x^3\hat{\mathbf{x}}\hat{\mathbf{z}}\\ \alpha_y^1\hat{\mathbf{y}}\hat{\mathbf{x}} & \alpha_y^2\hat{\mathbf{y}}\hat{\mathbf{y}} & \alpha_y^3\hat{\mathbf{y}}\hat{\mathbf{z}}\\ \alpha_z^1\hat{\mathbf{z}}\hat{\mathbf{x}} & \alpha_z^2\hat{\mathbf{z}}\hat{\mathbf{y}} & \alpha_z^3\hat{\mathbf{z}}\hat{\mathbf{z}}\end{bmatrix} \tag{A-6}$$

$$=\begin{array}{l}\beta_x(\alpha_x^1\hat{\mathbf{x}}+\alpha_x^2\hat{\mathbf{y}}+\alpha_x^3\hat{\mathbf{z}})+\ \beta_y(\alpha_y^1\hat{\mathbf{x}}+\alpha_y^2\hat{\mathbf{y}}+\alpha_y^3\hat{\mathbf{z}})+\\ \beta_z(\alpha_z^1\hat{\mathbf{x}}+\alpha_z^2\hat{\mathbf{y}}+\alpha_z^3\hat{\mathbf{z}})\end{array} \tag{A-7}$$

$$=\begin{array}{l}(\beta_x\alpha_x^1+\beta_y\alpha_y^1+\beta_z\alpha_z^1)\hat{\mathbf{x}}+\ (\beta_x\alpha_x^2+\beta_y\alpha_y^2+\beta_z\alpha_z^2)\hat{\mathbf{y}}+\\ (\beta_x\alpha_x^3+\beta_y\alpha_y^3+\beta_z\alpha_z^3)\hat{\mathbf{z}}\ ,\end{array} \tag{A-8}$$

where

$$\hat{\mathbf{e_i}}\cdot\hat{\mathbf{e_i}}\hat{\mathbf{e_j}}=\hat{\mathbf{e_j}},\quad \text{where } i,j=1,2,3\ \text{, and}$$
$$\hat{\mathbf{e_i}}\cdot\hat{\mathbf{e_j}}\hat{\mathbf{e_p}}=0,\quad \text{where } i,j,p=1,2,3 \text{ and } i\neq j.$$

An anterior vector product is defined as

$$\overline{\beta}(x,y,z)\times\overline{\overline{\mathscr{G}}}(x,y,z)=(\beta_x\hat{\mathbf{x}}+\beta_y\hat{\mathbf{y}}+\beta_z\hat{\mathbf{z}})\times\begin{bmatrix}\alpha_x^1\hat{\mathbf{x}}\hat{\mathbf{x}} & \alpha_x^2\hat{\mathbf{x}}\hat{\mathbf{y}} & \alpha_x^3\hat{\mathbf{x}}\hat{\mathbf{z}}\\ \alpha_y^1\hat{\mathbf{y}}\hat{\mathbf{x}} & \alpha_y^2\hat{\mathbf{y}}\hat{\mathbf{y}} & \alpha_y^3\hat{\mathbf{y}}\hat{\mathbf{z}}\\ \alpha_z^1\hat{\mathbf{z}}\hat{\mathbf{x}} & \alpha_z^2\hat{\mathbf{z}}\hat{\mathbf{y}} & \alpha_z^3\hat{\mathbf{z}}\hat{\mathbf{z}}\end{bmatrix} \tag{A-9}$$

$$=\begin{bmatrix}\alpha_x^1(-\beta_y\hat{\mathbf{x}}-\beta_z\hat{\mathbf{y}})\hat{\mathbf{x}} & \alpha_x^2(-\beta_y\hat{\mathbf{x}}-\beta_z\hat{\mathbf{y}})\hat{\mathbf{y}} & \alpha_x^3(-\beta_y\hat{\mathbf{x}}-\beta_z\hat{\mathbf{y}})\hat{\mathbf{z}}\\ \alpha_y^1(\beta_x\hat{\mathbf{z}}-\beta_z\hat{\mathbf{x}})\hat{\mathbf{x}} & \alpha_y^2(\beta_x\hat{\mathbf{z}}-\beta_z\hat{\mathbf{x}})\hat{\mathbf{y}} & \alpha_y^3(\beta_x\hat{\mathbf{z}}-\beta_z\hat{\mathbf{x}})\hat{\mathbf{z}}\\ \alpha_z^1(-\beta_x\hat{\mathbf{y}}+\beta_y\hat{\mathbf{x}})\hat{\mathbf{x}} & \alpha_z^2(-\beta_x\hat{\mathbf{y}}+\beta_y\hat{\mathbf{x}})\hat{\mathbf{y}} & \alpha_z^3(-\beta_x\hat{\mathbf{y}}+\beta_y\hat{\mathbf{x}})\hat{\mathbf{z}}\end{bmatrix}. \tag{A-10}$$

and further simplified. As an example, the anterior vector product of $\beta(x,y,z)$ and the

dyadic identity, $\overline{\overline{I}}$, will be performed. This vector product is defined as

$$\overline{\beta}(x,y,z) \times \overline{\overline{I}}(x,y,z) = (\beta_x \hat{\mathbf{x}} + \beta_y \hat{\mathbf{y}} + \beta_z \hat{\mathbf{z}}) \times \begin{bmatrix} \alpha_x^1 \hat{\mathbf{x}}\hat{\mathbf{x}} & 0 & 0 \\ 0 & \alpha_y^2 \hat{\mathbf{y}}\hat{\mathbf{y}} & 0 \\ 0 & 0 & \alpha_z^3 \hat{\mathbf{z}}\hat{\mathbf{z}} \end{bmatrix} \tag{A-11}$$

$$= \begin{bmatrix} \alpha_x^1(-\beta_y \hat{\mathbf{z}} + \beta_z \hat{\mathbf{y}})\hat{\mathbf{x}} & 0 & 0 \\ 0 & \alpha_y^2(\beta_x \hat{\mathbf{z}} - \beta_z \hat{\mathbf{x}})\hat{\mathbf{y}} & 0 \\ 0 & 0 & \alpha_z^3(-\beta_x \hat{\mathbf{y}} + \beta_y \hat{\mathbf{x}})\hat{\mathbf{z}} \end{bmatrix} \tag{A-12}$$

$$= \begin{bmatrix} 0 & \alpha_x^1 \beta_z \hat{\mathbf{y}}\hat{\mathbf{x}} & -\alpha_x^1 \beta_y \hat{\mathbf{z}}\hat{\mathbf{x}} \\ -\alpha_x^1 \beta_z \hat{\mathbf{x}}\hat{\mathbf{y}} & 0 & \alpha_y^2 \beta_x \hat{\mathbf{z}}\hat{\mathbf{y}} \\ \alpha_z^3 \beta_y \hat{\mathbf{x}}\hat{\mathbf{z}} & -\alpha_z^3 \beta_x \hat{\mathbf{y}}\hat{\mathbf{z}} & 0 \end{bmatrix}. \tag{A-13}$$